Cell Reports

Article

The human CNOT1-CNOT10-CNOT11 complex forms a structural platform for protein-protein interactions

Graphical abstract

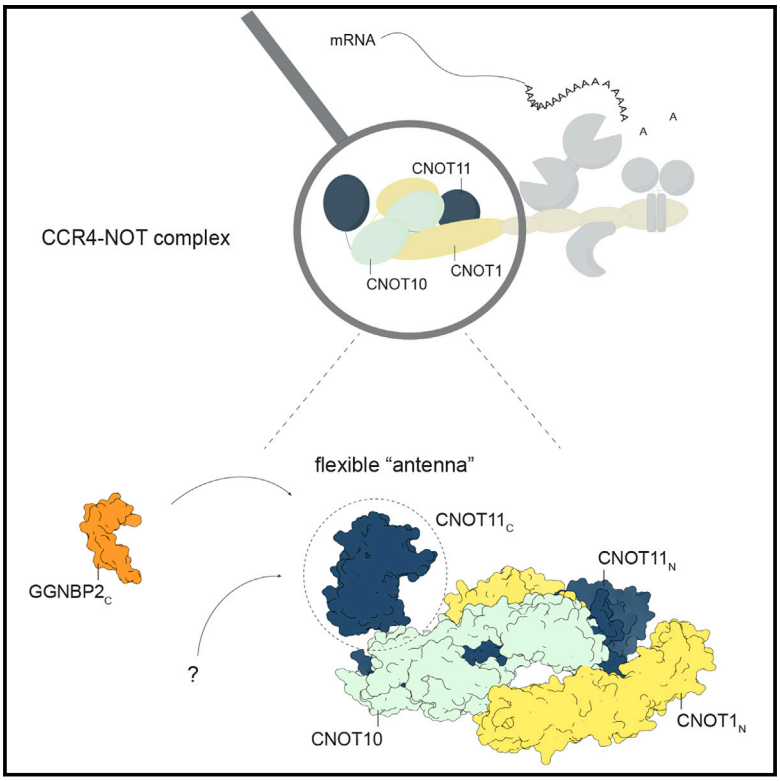

Highlights

- Structure of human CNOT1-CNOT10-CNOT11 reveals the CCR4-NOT N-terminal module
- The structured core is formed by intertwined interactions of CNOT1, CNOT10, and CNOT11
- The CNOT11 C-terminal region forms a protruding and highly conserved antenna domain
- The antenna domain directly binds the GGNBP2 effector protein in cells and *in vitro*

Authors

Fabienne Mauxion, Jérôme Basquin, Sevim Ozgur, ..., Ingmar Schäfer, Bertrand Séraphin, Elena Conti

Correspondence

mauxion@igbmc.fr (F.M.), basquin@biochem.mpg.de (J.B.), seraphin@igbmc.fr (B.S.), conti@biochem.mpg.de (E.C.)

In brief

The evolutionary conserved CCR4-NOT complex functions in the cytoplasm as the main mRNA deadenylase in both constitutive mRNA turnover and regulated mRNA decay pathways. Using different structural approaches, Mauxion et al. obtained high-resolution data revealing the architecture of the human N-terminal module (CNOT1, CNOT10, and CNOT11) and identified interacting partner.

Mauxion et al., 2023, Cell Reports *42*, 111902
January 31, 2023
https://doi.org/10.1016/j.celrep.2022.111902

CellPress

Cell Reports

CellPress
OPEN ACCESS

Article

The human CNOT1-CNOT10-CNOT11 complex forms a structural platform for protein-protein interactions

Fabienne Mauxion,[2,4,*] Jérôme Basquin,[1,4,*] Sevim Ozgur,[1] Marion Rame,[2,3] Jana Albrecht,[1] Ingmar Schäfer,[1] Bertrand Séraphin,[2,*] and Elena Conti[1,5,*]

[1]Department of Structural Cell Biology, Max Planck Institute of Biochemistry, Am Klopferspitz 18, Martinsried, Munich, Germany
[2]Institut de Génétique et de Biologie Moléculaire et cellulaire (IGBMC), Centre National de Recherche scientifique (CNRS) UMR 7104 – Institut National de santé et de Recherche Médicale (Inserm) U964 – Université de Strasbourg, 1 rue Laurent Fries, Illkirch, France
[3]Present address: Laboratoire ICube - UMR7357 Université de Strasbourg – CNRS, Institut de Physique Biologique, 1 place de l'hôpital, 67,000 Strasbourg, France
[4]These authors contributed equally
[5]Lead contact
*Correspondence: mauxion@igbmc.fr (F.M.), basquin@biochem.mpg.de (J.B.), seraphin@igbmc.fr (B.S.), conti@biochem.mpg.de (E.C.)
https://doi.org/10.1016/j.celrep.2022.111902

SUMMARY

The evolutionary conserved CCR4-NOT complex functions in the cytoplasm as the main mRNA deadenylase in both constitutive mRNA turnover and regulated mRNA decay pathways. The versatility of this complex is underpinned by its modular multi-subunit organization, with distinct structural modules actuating different functions. The structure and function of all modules are known, except for that of the N-terminal module. Using different structural approaches, we obtained high-resolution data revealing the architecture of the human N-terminal module composed of CNOT1, CNOT10, and CNOT11. The structure shows how two helical domains of CNOT1 sandwich CNOT10 and CNOT11, leaving the most conserved domain of CNOT11 protruding into solvent as an antenna. We discovered that GGNBP2, a protein identified as a tumor suppressor and spermatogenic factor, is a conserved interacting partner of the CNOT11 antenna domain. Structural and biochemical analyses thus pinpoint the N-terminal CNOT1-CNOT10-CNOT11 module as a conserved protein-protein interaction platform.

INTRODUCTION

The CCR4-NOT complex is a master regulator of gene expression conserved throughout the eukaryotic lineage.[1–4] Although CCR4-NOT was originally identified in *Saccharomyces cerevisiae* as a nuclear transcriptional repressor, a more prominent role in the shortening of the poly(A) tail of cytoplasmic mRNAs has emerged.[5,6] The poly(A) tail consists of a stretch of adenosines that is added to the 3′ end of the vast majority of mRNAs following transcription and is packaged with poly(A)-binding proteins to form a poly(A) ribonucleoprotein complex (RNP)[7]. In the cytoplasm, the poly(A) tail is gradually shortened during the lifetime of the transcript, first by the PAN2-PAN3 deadenylase and subsequently by the CCR4-NOT deadenylases, resulting in translational repression and/or mRNA degradation.[4,8] Besides its generic recruitment in constitutive mRNA turnover, CCR4-NOT is also exploited to elicit rapid deadenylation and decay of specific mRNAs.[4,8] Indeed, the CCR4-NOT complex has been shown to impact micro-RNA-mediated silencing in human cells and to regulate gene expression in early development of several model organisms.[1,9] The metazoan CCR4-NOT complex includes eight stably associated subunits named in mammals: CNOT1, CNOT2, CNOT3, CNOT6 (or its paralog CNOT6L), CNOT7 (or its paralog CNOT8), CNOT9, CNOT10, and CNOT11. In addition, mass spectrometry analyses of CCR4-NOT complexes purified from human cells consistently identify the mammalian-specific TNKS1BP1 protein,[10–12] but how the latter integrates into the complex remains to be investigated. The largest subunit, CNOT1 (Not1 in yeast), serves as the backbone of the CCR4-NOT complex and interacts with most other core subunits to form distinct structural and functional modules. CNOT1 can be broadly divided into N-terminal, middle, and C-terminal regions.

The middle region of CNOT1 ($CNOT1_M$) establishes the mRNA repressive function of CCR4-NOT.[13,14] At the center of the repressive region, a MIF4G-like domain (middle domain of initiation factor 4G) orchestrates the nuclease module of the complex by binding the deadenylase CNOT7/CNOT8 (orthologue of yeast Caf1), which in turn recruits CNOT6/CNOT6L (orthologue of yeast Ccr4),[15–17] the only core subunit that is recruited indirectly to CNOT1. The nuclease module is flanked at the N-terminus by another MIF4G-like domain[18] and at the C-terminus by a helical domain that binds the core subunit CNOT9, an armadillo-repeat protein (orthologue of yeast Caf40).[13,14] Essentially, all the core constituents of the middle region of CCR4-NOT can mediate

transient interactions with RNA-binding factors important for mRNA regulation, such as DDX6 and GW182/TNR6C for microRNA-mediated decay[13,14,19] or tristetraprolin (TTP), Roquin, and BTG/Tob for targeted degradation of mRNAs implicated in inflammation and cell proliferation control.[18,20–22]

The C-terminal module of CCR4-NOT is formed by the interaction of the C-terminal domain of CNOT1 ($CNOT1_C$) with CNOT2 and CNOT3 (orthologues of yeast Not2 and Not3/Not5).[23,24] The C-terminal module cross-talks with the translation machinery, interacting with slow-moving ribosomes.[25,26] In yeast, it also interacts with the ubiquitin ligase Not4, which is thought to activate proteasomal degradation when translation is halted.[27,28] In metazoans, the C-terminal module has been shown to bind Nanos, a translational repressor important for germ cell development.[29]

Last but not least is the N-terminal module of CCR4-NOT, which assembles around the N-terminal region of CNOT1 ($CNOT1_N$) and in metazoans includes CNOT10 and CNOT11 (also known as C2ORF29 in humans).[12,30] Purification of these two factors with endogenous CCR4-NOT complexes from human and *Drosophila* cells showed they are *bona fide* core subunits.[12,30] In *in vitro* assays with recombinant proteins, CNOT10 and CNOT11 were found to bind RNA and to accelerate deadenylation by CCR4-NOT.[31] At the cellular level, CNOT10 and CNOT11 were identified as regulators of interferon-responsive genes during infection of primary T cells with human immunodeficiency virus.[32] In mouse embryonic stem cells, depletion of CNOT10 was shown to promote the accumulation of specific transcripts.[33] Finally, in trypanosoma, deletion of the CNOT10 orthologue impaired the integrity of the CCR4-NOT complex, and consequently the degradation of many mRNAs.[34] Altogether, the precise organization and functions of the $CNOT1_N$-CNOT10-CNOT11 module remain enigmatic. In this work, we set out to elucidate the molecular basis with which the CNOT10 and CNOT11 subunits are incorporated into the CCR4-NOT complex and propose a model of how the N-terminal module serves as a recruiting platform for accessory factors.

RESULTS AND DISCUSSION

Reconstitution and structural analysis of the N-terminal module of the human CCR4-NOT complex

We reconstituted a recombinant version of the human $CNOT1_N$-CNOT10-CNOT11 ternary complex amenable to structural analysis (Figure 1A). Minor truncations were made to CNOT10 and CNOT11 to limit the presence of flexible and poorly conserved segments (Figure 1B). Thus, CNOT10 residues 1–714 (lacking the last 30 amino acids) and CNOT11 residues 61–510 (lacking an N-terminal part) were expressed. For simplicity, those are hereby referred to as CNOT10 and CNOT11, respectively. The entire N-terminal portion of CNOT1 was reconstituted (residues 1–685, hereby defined as $CNOT1_N$) (Figure 1B). This includes an ~30 kDa N-terminal region previously shown to be required for the interaction with CNOT11.[12,30] We determined the crystal structure of the corresponding ~220 kDa $CNOT1_N$-CNOT10-CNOT11 complex to 3.1 Å resolution via experimental phasing, allowing us to build most of the polypeptide chains *de novo* (Table S1). Only two areas were not readily interpretable at the atomic level in the refined map, although we could distinguish tubular features characteristic of α-helices (Figure S1A). Therefore, we obtained additional structural information to build these portions of the model. One area corresponded to the C-terminal domain of CNOT11. We purified and crystallized this domain independently (residues 323–510, referred to as $CNOT11_C$) and obtained its 2.2 Å resolution structure (Table S1), which could be placed as a rigid body in the density of the $CNOT1_N$-CNOT10-CNOT11 complex. The second area of lower resolution features corresponded to the C-terminus of $CNOT1_N$. Here, we used AlphaFold predictions to model the $CNOT1_N$ C-terminal helices (residues 549–685) and complete the model.

Altogether, the structural approaches resulted in a complete structural model of the $CNOT1_N$-CNOT10-CNOT11 module (Figure 1C). Briefly, a heterodimer formed by CNOT10 and CNOT11 is at the center of the complex. CNOT11 is a multidomain protein characterized by a globular α-helical domain ($CNOT11_N$, residues 61–276), an extended segment ($CNOT11_M$, residues 277–322) and a C-terminal domain ($CNOT11_C$, residues 323–510), previously known as domain-of-unknown-function 2363 (DUF 2363). $CNOT11_C$ is formed by a stack of five α-helical HEAT repeats, similar to the fold of other MIF4G-like domains in CNOT1.[15,18,17] CNOT10 is a tetratricopeptide repeat (TPR) protein, with 13 TPR repeats stacking against each other to form an elongated solenoid of roughly one and a half superhelical turns. The CNOT10 solenoid wraps around the extended $CNOT11_M$ segment and packs against the $CNOT11_N$ globular domain. Finally, the CNOT1 N-terminal region folds into two distinct helical HEAT-repeat domains (CNOT1 MIF4G-like domain 1, residues 1–230, and domain 2, residues 250–660) that are arranged in a U-shaped conformation around CNOT10-$CNOT11_{N-M}$. We refer to $CNOT1_N$-CNOT10-$CNOT11_{N-M}$ as the structured core of the CCR4-NOT N-terminal module. In the crystal structure, we observed loose interactions between $CNOT1_N$-CNOT10-$CNOT11_{N-M}$ and the $CNOT11_C$ MIF4G-like domain, but analysis of the lattice suggested that such positioning was likely due to crystal packing, in turn suggesting that $CNOT11_C$ may not be an integral part of the structured core. To test and confirm this, we analyzed the $CNOT1_N$-CNOT10-CNOT11 complex by single-particle cryo-electron microscopy (cryo-EM). The cryo-EM reconstruction we obtained at 4 Å resolution showed density corresponding to the structured core where we could readily place the $CNOT1_N$-CNOT10-$CNOT11_{N-M}$ atomic model we had built from the crystallographic data (Figure S1C). No ordered density was present for the $CNOT11_C$ domain, supporting the notion that this highly conserved domain is attached to the core complex as a flexible "antenna." Below, we first describe the $CNOT1_N$-CNOT10-$CNOT11_{N-M}$ structured core and then proceed to report on the structure and function of the $CNOT11_C$ "antenna" domain.

Intertwined interactions form the structured core of $CNOT1_N$-CNOT10-CNOT11

The structured core of $CNOT1_N$-CNOT10-$CNOT11_{N-M}$ has a multi-layered structure formed by conserved intermolecular interfaces (Figure 1C). The inner layer is the superhelical CNOT10-$CNOT11_M$ assembly. $CNOT11_M$ threads in an antiparallel orientation along the concave surface of the CNOT10 TPR

Please cite this article in press as: Mauxion et al., The human CNOT1-CNOT10-CNOT11 complex forms a structural platform for protein-protein interactions, Cell Reports (2022), https://doi.org/10.1016/j.celrep.2022.111902

CellPress
OPEN ACCESS

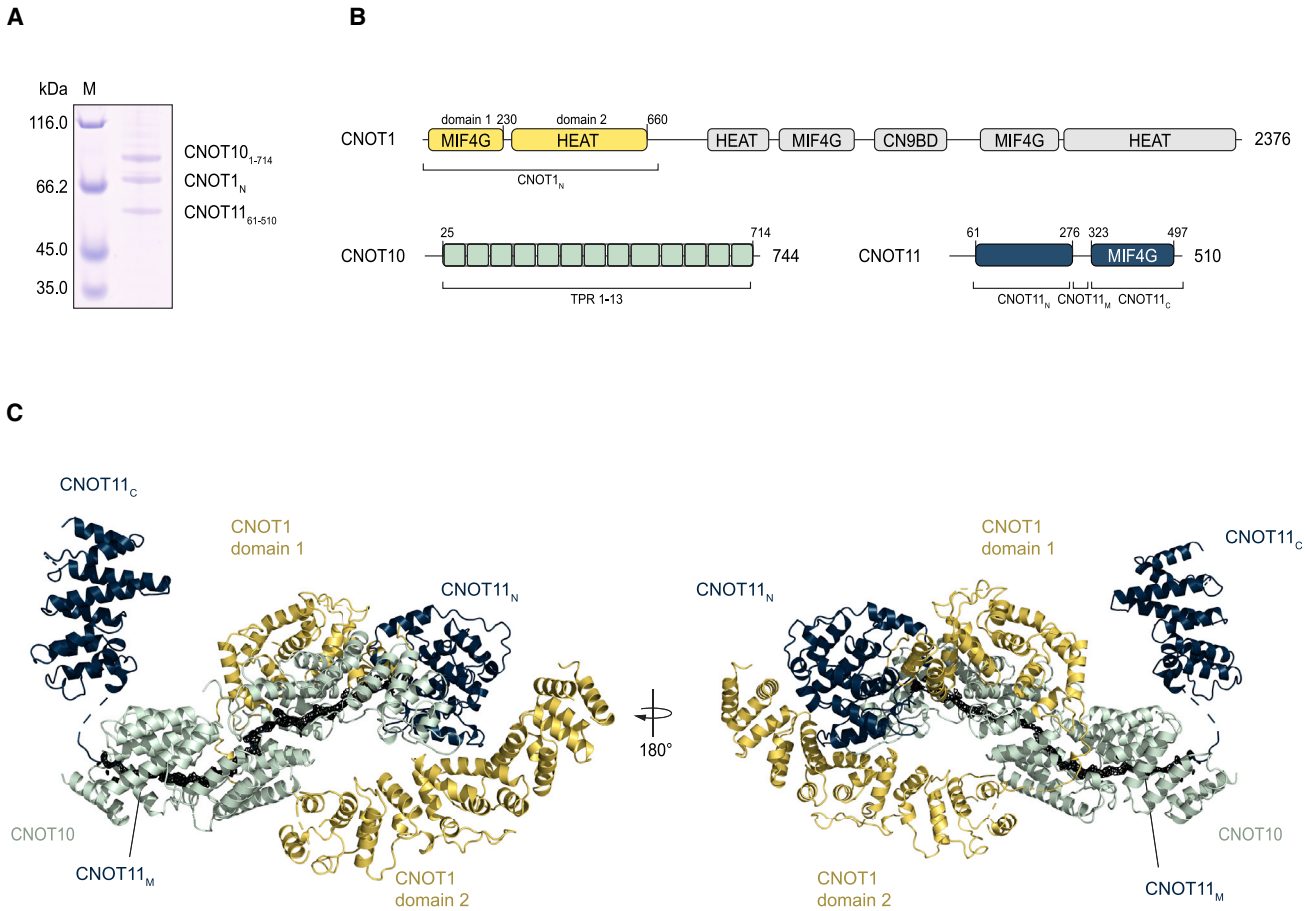

Figure 1. Structure of the N-terminal module of the human CCR4-NOT complex: A structured core with an antenna domain

(A) Coomassie-stained SDS-PAGE analysis of the purified recombinant sample of the human CNOT1$_N$-CNOT10-CNOT11 complex used for crystal structure determination. The complex corresponds to the N-terminal module of CCR4-NOT and includes only the N-terminal region of the scaffold protein CNOT1$_N$.

(B) Schematic representation of the domain organization of human CNOT1$_N$ (yellow), CNOT10 (light green), and CNOT11 (blue). The structured domains are indicated as rectangles and linker regions are shown as black lines. Labeling of the different portions of the proteins corresponds to the structural analysis, as discussed in the text. In particular, the N-terminal, middle, and C-terminal region of CNOT11 are indicated with the corresponding suffix N, M, C. HEAT,[35] TPR,[36] MIF4G[37]; C9BD (CNOT9 binding domain).

(C) Crystal structure of the CNOT1$_N$-CNOT10-CNOT11 complex in two different orientations, colored and labeled as in (B). The model of the structured core (CNOT1$_N$-CNOT10-CNOT11$_{M-N}$) is refined to 3.1 Å resolution. Due to the apparent flexible connection to the core, the model of the "antenna" domain (CNOT11$_C$) was determined separately at 2.2 Å resolution and fitted in the density of the ternary complex.

solenoid, extending over 90 Å and contributing to the hydrophobic core of the superhelix. The CNOT10-CNOT11$_M$ interaction is characterized by three major hotspots of conserved hydrophobic contacts: an apolar patch at the beginning of the CNOT10 solenoid (TPRs 1–2) binds CNOT11$_M$ Trp312 and Met316 (Figure 2A), another apolar patch in the middle of the solenoid (TPRs 6–8) binds CNOT11$_M$ Leu298 and Trp300 (Figure 2B), and a third apolar patch at the end of the solenoid (TPRs 9–13) binds a proline-rich segment of CNOT11$_M$ (Phe284, Pro287-290, Leu291) (Figure 2C) (see amino acid conservation in Figure S2). In addition, the CNOT10-CNOT11$_M$ interactions involve electrostatic contacts (for example, CNOT11$_M$ Asp296 - CNOT10 Arg390 in the central patch and CNOT11$_M$ Arg286 - CNOT10 Glu579 in the last patch) as well as polar contacts (Figures 2B and 2C). A set of conserved asparagine residues on the CNOT10 concave surface engage with the CNOT11$_M$ backbone, particularly in the first and second patches (Asn66-115 and Asn298-360, respectively, Figures 2A and 2B), and in-between the proline-binding sites of the third patch (Asn648, Figure 2C), with a similar interaction strategy previously shown to extend and orient polypeptides along protein-binding sites.[38] Most of the amino acids involved in interactions within CNOT10 - CNOT11$_M$ are highly conserved, including in the more divergent orthologues such as *Drosophila melanogaster* (Figure S2).

The CNOT10 - CNOT11$_M$ superhelical assembly is surrounded by two outer layers, probably explaining why prior association of CNOT10 with CNOT11 is necessary for integration in the CCR4-NOT complex. One layer is formed by CNOT1$_N$ domain 1 and CNOT11$_N$. These two domains pack against each other via extensive hydrophobic contacts mediated by the N-terminus of the CNOT1$_N$ MIF4G-like domain (including Met1 and Leu3) and a prominent pocket in CNOT11$_N$ (including Ala147 and Val109)

Please cite this article in press as: Mauxion et al., The human CNOT1-CNOT10-CNOT11 complex forms a structural platform for protein-protein interactions, Cell Reports (2022), https://doi.org/10.1016/j.celrep.2022.111902

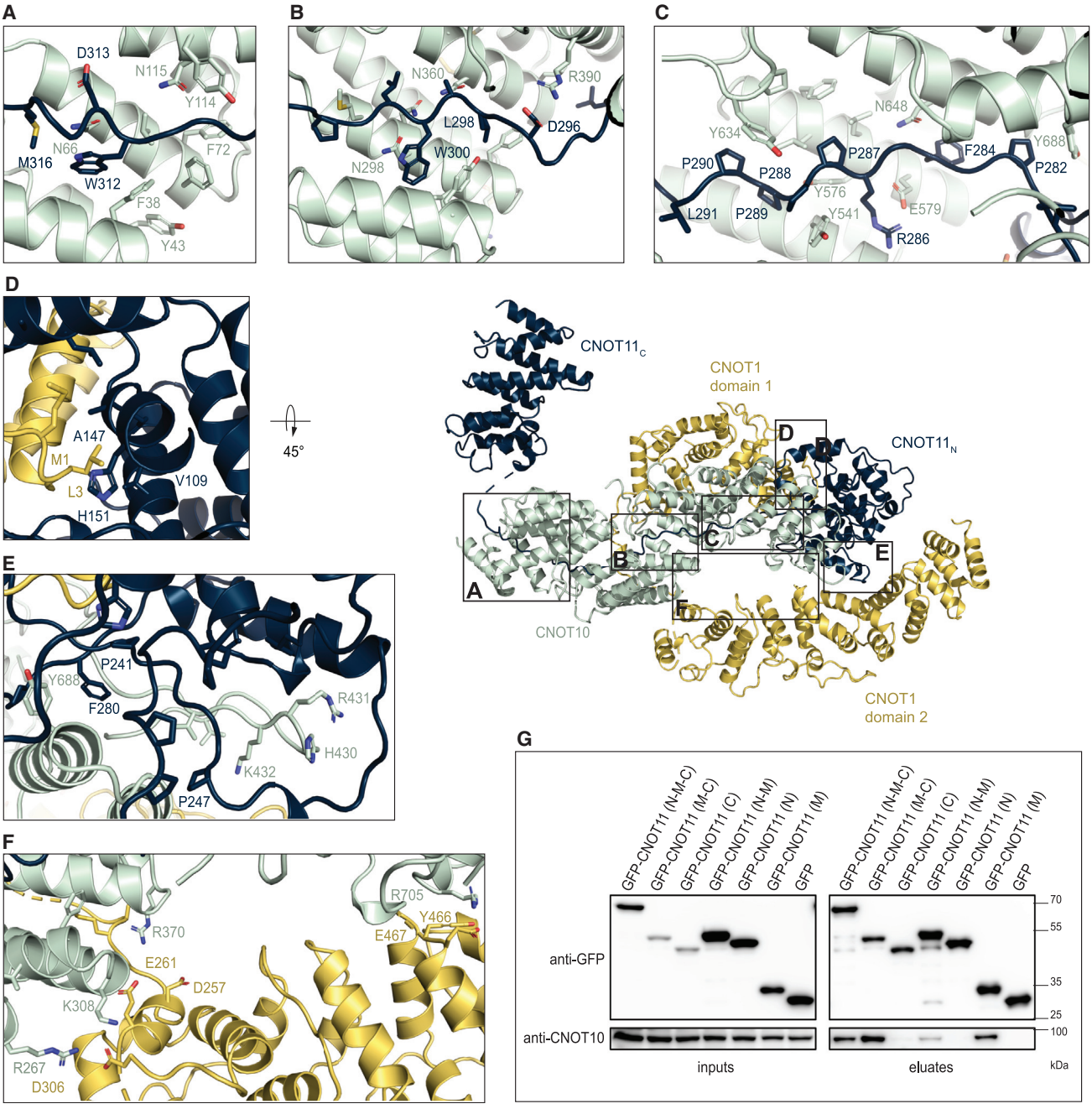

Figure 2. The structured core of the CNOT1$_N$-CNOT10-CNOT11 complex is formed by evolutionary conserved interactions

(A–F) Zoom-in views of the major structural interactions in the CNOT1$_N$-CNOT10-CNOT11$_{N-M}$ core of the CCR4-NOT N-terminal module. The individual views are also indicated in the context of the entire structure. (A–C) highlight conserved interactions within the inner layer of the complex comprising the extended CNOT11$_M$ region and the CNOT10 TPR superhelix. The interactions with the two outer layers are shown in (D and E) (CNOT1$_N$ domain 1, CNOT11, and CNOT10) and (F) (CNOT1$_N$ domain 2 and CNOT10). The evolutionary conservation of the interactions is shown in Figures S2A–S2C.

(G) Biochemical validation of the structural analysis. Co-immunoprecipitation of endogenous CNOT10 with GFP-tagged CNOT11 truncated proteins. HEK293 cells were transfected with plasmids expressing GFP-tagged human CNOT11 fusion proteins or empty GFP expression vector. Proteins were immunoprecipitated with GFP-Trap magnetic beads and the co-precipitation was analyzed by western blotting. For some constructs, limited CNOT11 degradation during immunoprecipitation generated additional lower molecular-weight bands.

Please cite this article in press as: Mauxion et al., The human CNOT1-CNOT10-CNOT11 complex forms a structural platform for protein-protein interactions, Cell Reports (2022), https://doi.org/10.1016/j.celrep.2022.111902

CellPress
OPEN ACCESS

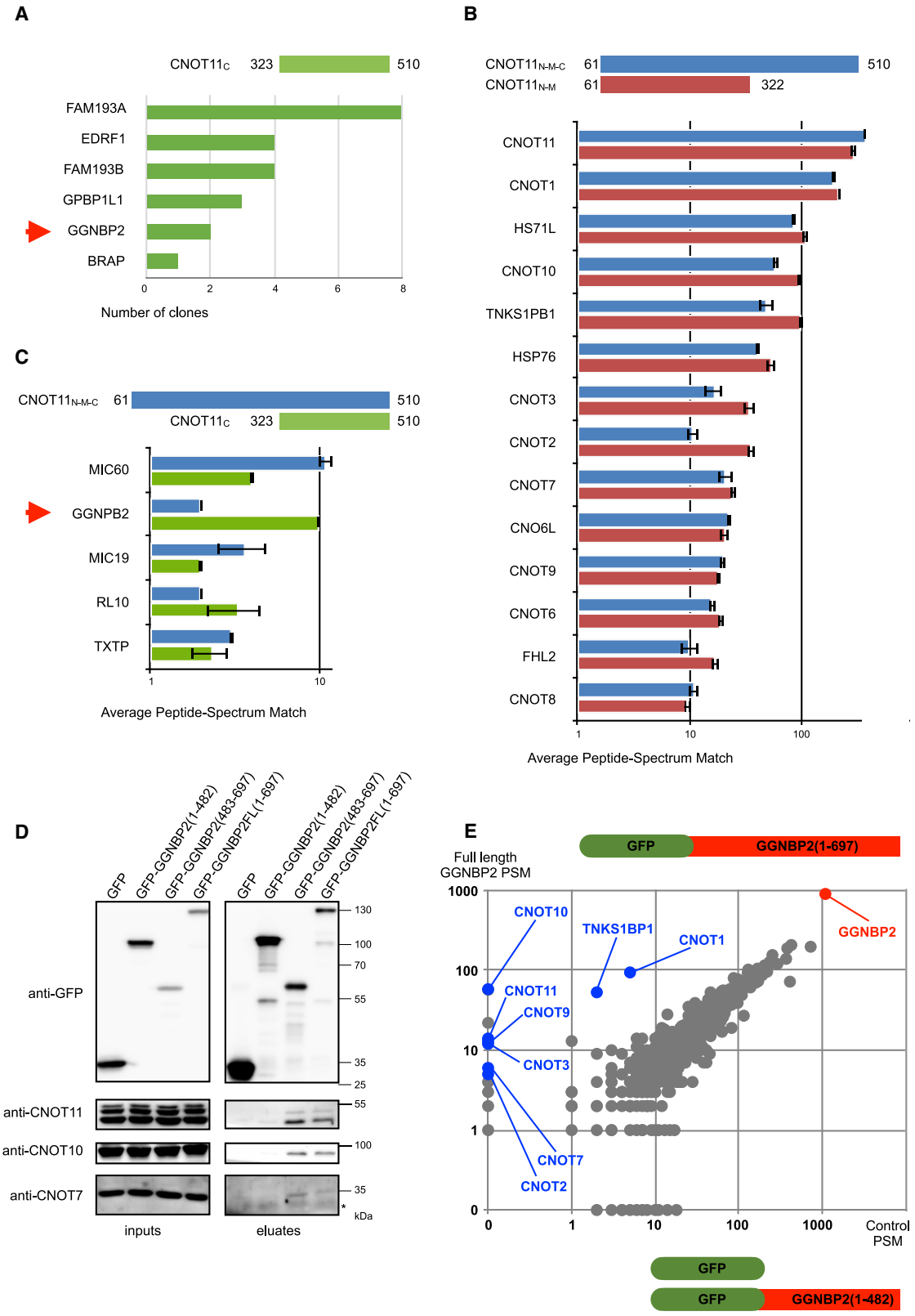

(legend on next page)

(Figure 2D). In addition, CNOT11$_N$ interacts with TPR13 (Figure 2E). The interaction appears to be stabilized by a 20-residue-long intra-repeat loop of CNOT10 (residues 421–443) that extends from TPR9 over to TPR13 with well-defined density, wedging between CNOT11$_N$ and CNOT11$_M$ (Figure 2E).

The other outer layer is formed by CNOT1$_N$ domain 2. This domain binds on the opposite surface of the superhelix, engaging TPRs 6–8 and TPR13, mainly with electrostatic contacts (Figure 2F) that are conserved, albeit not in more divergent orthologues such as *D. melanogaster* (Figures S2A and S2C). Consistently, human CNOT1$_N$ domain 1 has been shown to be sufficient and necessary for CNOT10-CNOT11 binding in contrast to CNOT1$_N$ domain 2.[12] CNOT1$_N$ domain 1 and domain 2 are connected by an extended linker that crosses over the superhelix, effectively connecting the two opposite outer layers.

The structural analysis was surprising in that we found that the CNOT11$_{N-M}$ domains mediate the intermolecular interactions in the complex rather than CNOT11$_C$, as had instead been suggested based on biochemical studies that had relied heavily on sequence conservation between human and fly orthologues.[30] To validate the structural data, we performed pull-down assays with CNOT11 truncation mutants (Figure 2G). GFP-tagged versions of the CNOT11 truncation mutants were transfected in HEK293 cells, and pull-down assays with GFP nanobodies were used to detect co-precipitated proteins visualized by western blot. As a positive control, GFP-CNOT11$_{N-M-C}$ was able to pull down CNOT10; as a negative control, GFP alone did not co-precipitate this factor. GFP-CNOT11$_{M-C}$ and GFP-CNOT11$_{N-M}$ co-precipitated CNOT10. However, no co-precipitation was detected in the case of GFP-CNOT11$_N$ or GFP-CNOT11$_C$. In contrast, GFP-CNOT11$_M$ was able to precipitate CNOT10. These results indicate that the CNOT11$_M$ is not only necessary but also sufficient for formation of the complex, consistent with structural data. Independent data obtained by two-hybrid assays confirmed that CNOT11$_{N-M-C}$, but not CNOT11$_C$, interacts with CNOT10 (Figure S3). Together, these data using structure-based truncations confirm that the conserved CNOT11$_C$ domain is not required for incorporation of CNOT11 in the CCR4-NOT complex.

The C-terminal domain of CNOT11 is an antenna for protein recruitment

The structural and biochemical data above raised the question as to the function(s) of the CNOT11$_C$ MIF4G-like domain, the highly conserved antenna domain of the CNOT1$_N$-CNOT10-CNOT11 complex (Figure S2B). Other MIF4G-like domains in the CCR4-NOT complex have been shown to recruit either a DEAD-box ATPase (DDX6[15,17]) or a largely unstructured protein (e.g., TTP[18]). Reasoning that the CNOT11$_C$ MIF4G-like domain may also mediate additional protein-protein interactions, we proceeded to identify putative interactors. A two-hybrid screen was performed: the sequence encoding CNOT11(323-510) (i.e., CNOT11$_C$) was fused to the LexA DNA-binding domain and used to screen a human placenta cDNA library. Clones encoding fragments of six different proteins fused to the Gal4 transcription activation domain were retrieved, some up to eight times (Figure 3A). None of the retrieved sequences encoded for subunits of the CCR4-NOT complex, in line with our structural and interaction data. Among the six top-scoring interaction partners there is no known RNA-binding protein or DEAD-box helicase. We therefore followed a complementary approach to delineate the most promising candidate and performed affinity purification-mass spectrometry (AP-MS) experiments.

For the AP-MS experiments, we used constructs encoding the TAP (tandem affinity purification) tag fused at the N-terminus of CNOT11$_{N-M-C}$, CNOT11$_{N-M}$, or CNOT11$_C$. A construct expressing the TAP tag alone was used to monitor background. These constructs were transiently transfected in HEK293 cells, as MS data (http://www.peptideatlas.org/) indicated that these cells normally express all factors identified in the two-hybrid screen. Proteins bound to the baits were isolated by TAP affinity purification. Recovered proteins were digested with trypsin, and peptides fractionated by liquid chromatography before identification by MS. In the case of CNOT11$_{N-M-C}$ and CNOT11$_{N-M}$, the most frequently identified polypeptides were subunits of the CCR4-NOT complex (Figure 3B).

We then focused on the proteins co-purifying specifically with CNOT11$_{N-M-C}$ and CNOT11$_C$, that is with constructs including the conserved C-terminal domain of CNOT11 (Figure 3C). Of the several putative partners in the AP-MS experiments,

Figure 3. The antenna domain of CNOT11 mediates the recruitment of GGNBP2 to CCR4-NOT

(A) CNOT11$_C$ protein partners from a human placenta cDNA library identified in a yeast two-hybrid screen. The number of clones encoding fusions with different ORF is shown. The common region found in the different clones encoding CNOT11$_C$ partners is: BRAP (113–490), EDRF1 (283–595), FAM193A (1,155–1,240), FAM193B (680–822), GGNBP2 (483–697), and GPBP1L1 (307–462). An arrow marks GGNBP2 also identified by affinity purification-mass spectrometry.

(B) Identification of proteins co-purifying with the N-terminus of CNOT11 by mass spectrometry. HEK293 cells were transfected with plasmids expressing TAP-tagged CNOT11 fusion proteins that were purified by two tandem affinity purification steps. Co-purified proteins were identified by mass spectrometry. Proteins found in control purification (such as keratins) were filtered out. The average number of Peptide-Spectrum Match (PSM) and standard deviation for the top 14 identified proteins in three mass spectrometry replicates for CNOT11$_{N-M-C}$ and CNOT11$_{N-M}$ are shown.

(C) Identification of proteins co-purifying with the C-terminus of CNOT11 by mass spectrometry. Protocol similar to (B). The average number of Peptide-Spectrum Match (PSM) and standard deviation for the top 6 identified proteins in three mass spectrometry replicates for CNOT11$_{N-M-C}$ and CNOT11$_C$ are shown. An arrow marks GGNBP2, also identified in the two-hybrid screen.

(D) Co-immunoprecipitation of endogenous CNOT7, CNOT10, and CNOT11 with GFP-tagged GGNBP2 proteins. HEK293 cells were transfected with plasmids expressing GFP-tagged human GGNBP2 fusion proteins (numbers in parentheses indicate amino acids included, FL = Full-Length), or empty GFP expression vector. Proteins were immunoprecipitated with GFP-Trap magnetic agarose beads and the co-precipitation was analyzed by western blotting on 8% PAGE. Note that CNOT11 always appears as multiple bands in cell lysates while overexpressed GFP-GGNBP2 often appears slightly degraded.

(E) Identification of proteins co-purifying with GFP-GGNBP2 by mass spectrometry. The plot compares the average number of PSM for each protein obtained in purification with GFP-GGNBP2FL (y axis) versus control purifications with GFP alone and GFP-GGNBP2(1-482) (x axis). GGNBP2 is indicated in red while subunits of the CCR4-NOT complex and partners are indicated in blue.

Please cite this article in press as: Mauxion et al., The human CNOT1-CNOT10-CNOT11 complex forms a structural platform for protein-protein interactions, Cell Reports (2022), https://doi.org/10.1016/j.celrep.2022.111902

CellPress
OPEN ACCESS

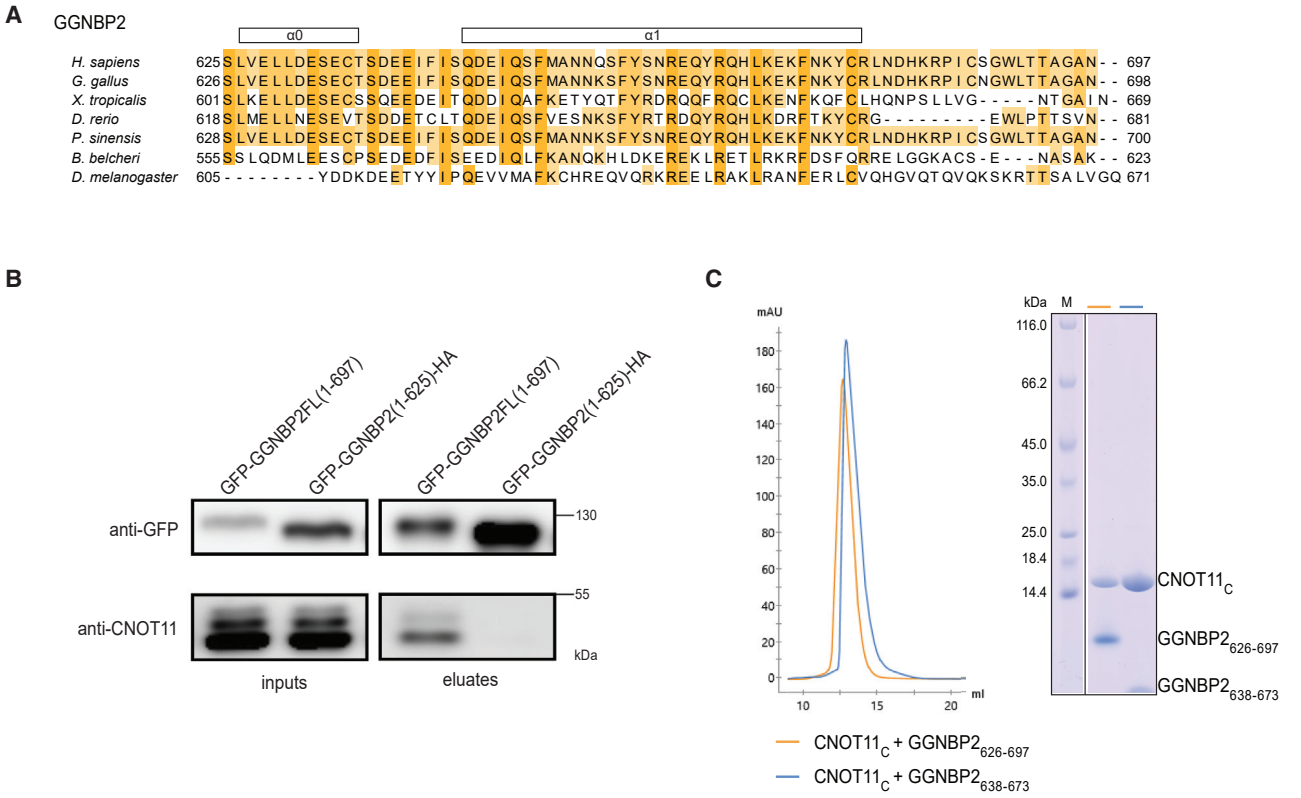

Figure 4. The CNOT11 antenna domain recognizes the C-terminal segment of GGNBP2

(A) Structure-based sequence alignment of CNOT11-binding domain of GGNBP2. Highlighted in dark and light orange are residues with high and medium conservation across the species shown. A schematic representation shows the position of the two α-helices with respect to the amino acid sequence.

(B) Co-immunoprecipitation of endogenous CNOT11 with GFP-tagged truncated GGNBP2 proteins. HEK293 cells were transfected with plasmids expressing GFP-tagged human GGNBP2 fusion proteins (numbers in parentheses indicate amino acids included, FL = Full-Length, GGNBP2 C-terminal residues were replaced by an HA tag in the GFP-GGNBP2(1-625)-HA construction). Proteins were immunoprecipitated with GFP-Trap magnetic agarose beads and the co-precipitation was analyzed by western blotting. Note that CNOT11 always appears as multiple bands in cell lysates.

(C) Reconstitution of the CNOT11-GGNBP2 interaction *in vitro* with recombinant proteins. Chromatogram from size-exclusion chromatography and corresponding Coomassie-stained SDS-PAGE analysis of the peak fraction shows the presence of a complex between $CNOT11_C$ and two C-terminal segments of

(legend continued on next page)

gametogenetin-binding protein 2 (GGNBP2, also known as ZNF403 or LCRG1) appeared as a strong candidate, as it was one of the proteins also independently identified in the two-hybrid screen (Figure 3A).

CNOT11 recruits the GGNBP2 protein to CCR4-NOT

We tested the putative interaction between $CNOT11_C$ and GGNBP2 by performing co-precipitation assays from HEK293 cells transfected with GFP-GGNBP2 fusion constructs. Pull-down assays with GFP nanobodies showed that full-length (FL) GGNBP2 could precipitate endogenous CNOT11 and its interacting partner CNOT10, as well as CNOT7 (Figure 3D). Since the two-hybrid screen performed with $CNOT11_C$ recovered a GGNBP2 fusion that included only the C-terminal region spanning residues 483–697, we tested the corresponding truncation mutants in the co-immunoprecipitation experiments. A GFP-tagged version of GGNBP2(483-697) was indeed sufficient to precipitate CNOT11, CNOT10, and CNOT7, while no interaction was observed with GGNBP2(1-482) (Figure 3D). MS analysis of the pull-down samples identified most subunits of the CCR4-NOT complex associated with GFP-GGNBP2FL but not with GFP alone or GFP-GGNBP2(1-482) (Figure 3E). These data confirm that GGNBP2 binds to CNOT11 in the context of the full CCR4-NOT complex *in vivo*.

The GGNBP2 483–697 region is predicted to contain an unstructured part followed by a C-terminal segment of about 70 residues with helical secondary structure elements[39] that are evolutionary conserved (Figures 4A and S2D). Co-immunoprecipitation assays using a C-terminally truncated GGNBP2 (GFP-GGNBP2(1-625)-HA) showed that the conserved C-terminal segment of GGNBP2 is essential for the interaction with endogenous CNOT11 (Figure 4B). Finally, we carried out size exclusion chromatography experiments with purified recombinant proteins, showing that a C-terminal segment of GGNBP2 (residues 626–697) and the $CNOT11_C$ domain interact directly (Figure 4C). Altogether, our data indicate that the 70 C-terminal residues of GGNBP2 are necessary and sufficient to bind $CNOT11_C$.

GGNBP2 wraps around the CNOT11 MIF4G-like domain via conserved interactions

The $CNOT11_C$ domain contains five HEAT repeats that pack in tandem to form the typical structure of MIF4G-like domains. An idiosyncratic feature of the $CNOT11_C$ structure is the presence of a specific set of evolutionary conserved residues that line different surfaces of this MIF4G-like domain. To understand if and how GGNBP2 could recognize these surfaces, we proceeded to determine the structure of a $CNOT11_C$-GGNBP2 complex. Co-crystallization experiments with the entire C-terminal segment of GGNBP2 (residues 626–697) were not successful. However, we could identify a smaller fragment (residues 638–673) capable of forming a complex with $CNOT11_C$ (Figure 4C) and yielding diffracting crystals. We determined the crystal structure of this complex to 2.4 Å resolution, showing well-defined density for essentially all the GGNBP2 residues in this fragment (Table S1). Inspection of the structure also showed that a significant part of the $CNOT11_C$ surface was engaging in crystal lattice contacts, casting doubt on whether this surface is rendered inaccessible to additional potential interactions. With the very recent release of AlphaFold-Multimer for predicting protein complexes,[40] we tested artificial-intelligence-based predictions with the longer version of the GGNBP2 C-terminal segment. AlphaFold-Multimer prediction recapitulated the major interaction hotspot we determined in the experimentally derived structural data (Figures 4D and S4A) and also allowed us to extend and complete the atomic model in areas hampered by crystal lattice contacts. Combined together, the complete model of the $CNOT11_C$-binding domain of GNPB2 encompasses residues 626–679 ($GGNBP2_C$) (Figure 4D).

The most prominent feature of $GGNBP2_C$ is a long and bent α-helix (α1) that binds along the convex surface the $CNOT11_c$ MIF4G-like domain (Figure 4D). The major interaction hotspot is between the first six helical turns of $GGNBP2_C$ helix α1 and the last two repeats of $CNOT11_C$. A patch of conserved hydrophobic residues on HEAT 5 (CNOT11 Ile472, Ala476, Ile479, Phe491) interacts with conserved hydrophobic residues of $GGNBP2_C$ helix α1 (Ile643, Phe651, Phe658, Tyr665) (Figure 5A, right panel). Furthermore, a negatively charged cleft between HEAT repeats 4–5 (Glu437, Glu473, Glu480) engages a positively charged region of helix α1 of $GGNBP2_C$ (Arg662, Arg666) (Figure 5A, left panel). From AlphaFold predictions, the cleft in the adjacent repeat (between HEAT 3–4) binds another set of conserved hydrophobic residues in the last turns of $GGNBP2_C$ helix α1 (Leu669, Phe673, Cys677) (Figure S4). Also from AlphaFold predictions, on the concave side of the MIF4G-like domain, CNOT11 HEAT 3–5 interact with hydrophobic and charged residues of $GGNBP2_C$ helix α0 (Figure S4). All interfaces are characterized by conserved residues involved in interactions (Figures S2 and S4B). Albeit also conserved, the contribution of $GGNBP2_C$ helix α0 (residues 626–636) is not crucial for CNOT11 binding (Figure 4C).

To biologically validate the mode of recruitment of GGNBP2 by CNOT11, we engineered structure-based mutants at the major interaction hotspot and tested them in yeast two-hybrid assays. A mutant of CNOT11 with substitutions of two central hydrophobic residues (A476E, F491D) was still able to interact with CNOT10, but interaction with GGNBP2 was not detectable above background (Figure 5B). Correspondingly, we tested mutations of GGNBP2 residues recognized at this hotspot (I643A, F651R, and/or F658D). Combinations of these substitutions in the GGNBP2 construct (483–697) for two-hybrid yeast assays reduced β-galactosidase levels by 4- to 6-fold as a result of interaction with $CNOT11_{N\text{-}M\text{-}C}$ (Figure 5C). To further validate these findings, mammalian expression constructs encoding mutated

GGNBP2: residues 626–697 and the truncation mutant encompassing residues 638–673 that was still able to interact with $CNOT11_C$ and that was used for the crystal structure determination of the complex.

(D) Overall structure of the complex between $CNOT11_C$ (in blue) and $GGNBP2_C$ (in orange, the atomic model from the crystal structure; in red, superposed the model from AlphaFold predictions, Figure S4A). The HEAT repeats of $CNOT11_C$ are labeled, as well as the $GGNBP2_C$ helices (α0 and α1). On the right, the $CNOT11_C$ - $GGNBP2_C$ complex (atomic model from the crystal structure) is positioned in the $CNOT1_N$-CNOT10-CNOT11 module.

Please cite this article in press as: Mauxion et al., The human CNOT1-CNOT10-CNOT11 complex forms a structural platform for protein-protein interactions, Cell Reports (2022), https://doi.org/10.1016/j.celrep.2022.111902

CellPress
OPEN ACCESS

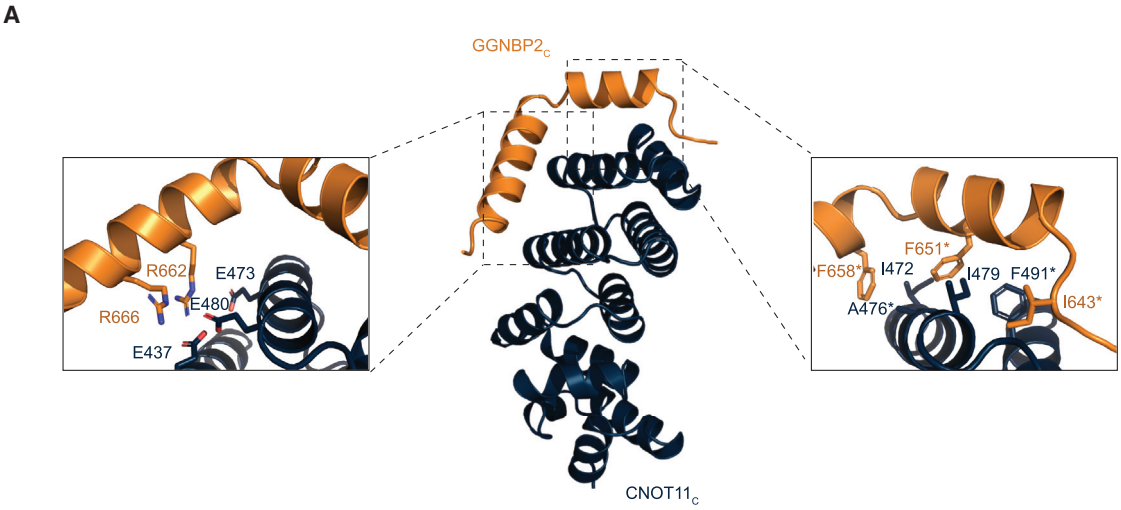

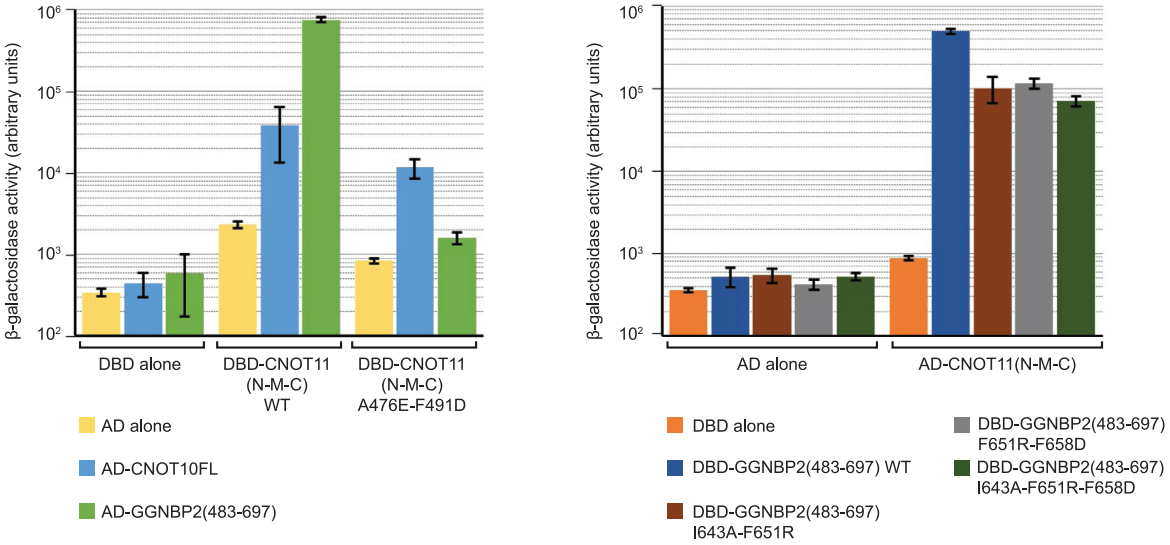

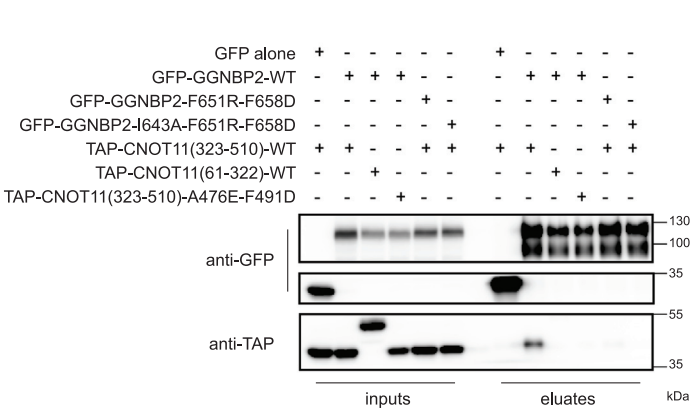

(legend on next page)

GFP-GGNBP2 or TAP-CNOT11 proteins were introduced into human HEK293 cells. Mutations led to complete abrogation of binding between GGNBP2 and CNOT11 (Figure 5D). These data confirm contacts observed in the CNOT11-GGNBP2 structure and demonstrate that the CNOT11 C-terminal domain acts as a platform to recruit GGNBP2.

Conclusions

The N-terminal module of the human CCR4-NOT complex is scaffolded by a solenoid formed by the TPR protein CNOT10 and an extended part of CNOT11 clamped within it. Two individual domains at the N-terminus of CNOT1 sandwich the solenoid, forming the outer layers of the CCR4-NOT N-terminal module and eventually connecting it via a linker to the following deadenylase and C-terminal modules of the complex. The hierarchy of interactions that we observe in the structure explains previous biochemical and functional data indicating that CNOT10 and CNOT11 need to be present simultaneously to form a stable complex with $CNOT1_N$.[12,30] The structural data also rationalize why CNOT10-CNOT11 have been observed to only assemble with the longest isoforms of CNOT1, and not with those having shorter N-termini.[12,30,32] Some variability in the fine organization of this module through evolution can be anticipated, as the $CNOT11_N$ domain that contributes to interaction with CNOT1 in human is absent from the *Drosophila* protein.[30] It remains unclear how CNOT10-CNOT11 may impact on the general deadenylase activity of the metazoan complex, as had been previously suggested.[31] Elucidating the structure of the entire CCR4-NOT complex will ultimately be required to understand if the individual modules interact and crosstalk with each other and, if so, how. Another aspect that remains unclear is the molecular basis for how a heterozygous *de novo* mutation of human CNOT1 Arg535 to Cys is connected to pancreatic agenesis and holoprosencephaly.[41,42] In our structure, this residue is exposed to solvent and is not involved in binding CNOT10 or CNOT11, suggesting it may impact a yet unknown interaction.

Unexpectedly, the structural analysis shows that the most conserved domain of CNOT11 is not involved in forming the core of the $CNOT1_N$-CNOT10-CNOT11 complex. Rather, the highly conserved C-terminal domain of CNOT11 folds into an independent MIF4G-like domain that projects out from the core of the N-terminal CCR4-NOT module as an antenna. We found that this domain serves as a platform for recruiting GGNBP2. GGNBP2 is an essential factor for spermatogenesis in mice[43,44] and it was also reported to act as a tumor suppressor in different human cancer cells.[45–48] It is tempting to speculate that the molecular mechanisms underpinning the essential functions of GGNBP2 in germ cell development and in inhibiting cell proliferation may relate to regulation of the stability or translation of specific RNA transcripts via its recruitment to CCR4-NOT. This concept of CNOT10-CNOT11 functioning in specific mRNA targeting would rationalize previous observations that depletions of CNOT10 and CNOT11 in human or *Drosophila* cells do not affect global mRNA decay.[12,30] Alternatively, we cannot exclude that GGNBP2 could affect transcription, or complex localization and dynamics. Sequence conservation and structure prediction suggest that GGNBP2 is likely to contain a globular N-terminal domain followed by an intrinsically disordered region preceding the $CNOT11_C$ interaction region. It is thus tempting to speculate that the GGNBP2 N-terminus binds specific factors, be it RNA or protein, and that it bridges these factors to the CCR4-NOT complex.

We believe it is unlikely that GGNBP2 may be the exclusive partner of the $CNOT11_C$ domain. Half of the CNOT11 MIF4G-like domain presents conserved solvent-exposed surfaces that are not used to bind GGNBP2 (Figure S4B), suggesting that these surfaces may function as a platform to recruit additional proteins. Interestingly, among the putative interactors we have identified in our assays (Figures 3A and 3C), at least one of them (FAM193A) yields reasonable predictions for $CNOT11_C$ binding using AlphaFold-Multimer. Future work will be directed at characterizing other evolutionary conserved interactions and functions of the CCR4-NOT N-terminal module and elucidating its integration with other parts of this large machinery.

Limitations of the study

We cannot exclude that tissue-specific or developmentally regulated interactors of $CNOT11_C$ have been missed by our strategy. On the structural side, further analyses will be required to understand the positioning of the $CNOT1_N$-CNOT10-CNOT11 in the full assembly.

STAR★METHODS

Detailed methods are provided in the online version of this paper and include the following:

- KEY RESOURCES TABLE
- RESOURCE AVAILABILITY

Figure 5. The GGNBP2 C-terminal segment wraps around the CNOT11 antenna domain with conserved interactions

(A) Zoom-in views of major structural interactions in the $CNOT11_C$-$GGNBP2_C$ complex. Labeled by asterisks in the top right panel are the CNOT11 residues Ala476 and Phe491 and the GGNBP2 residues Ile643, Phe651, and Phe658 that are mutated in the assays shown in (B–D).

(B) Interaction of CNOT11 wild-type or mutant (A476E, F491D) proteins with GGNBP2 in yeast two-hybrid assays. The host yeast strain was co-transformed with plasmids expressing the indicated LexA-DNA-Binding-Domain (DBD) and Gal4-Activating-Domain (AD) fusion proteins (numbers in parentheses indicate included amino acids; FL, full-length; WT, wild-type). Interaction between the different chimeric proteins indicated was assessed by β-galactosidase assays performed in duplicate. Activities are expressed in arbitrary units and plotted on a logarithmic scale. Three biological replicates were assayed and the average activity was plotted with standard deviation indicated as error bars.

(C) Interaction of GGNBP2 wild-type or mutant (I643A and/or F651R, F658D) proteins with CNOT11 in yeast two-hybrid assays. Protocol as in (B).

(D) Co-immunoprecipitation of wild-type (WT) and mutant CNOT11 with WT and mutant GGNBP2 proteins. HEK293 cells were co-transfected with plasmids expressing GFP-tagged human WT and mutant GGNBP2 proteins with TAP-tagged CNOT11 WT and mutant proteins (numbers in parentheses indicate amino acids included). Proteins were immunoprecipitated with GFP-Trap magnetic M-270 beads and the co-precipitation was analyzed by western blotting on 10% PAGE.

SUPPLEMENTAL INFORMATION

Supplemental information can be found online at https://doi.org/10.1016/j.celrep.2022.111902.

ACKNOWLEDGMENTS

We acknowledge our team members for support and suggestions, and Courtney Long for help with the manuscript. We are very grateful to the Crystallization Facility of the Max Planck Institute of Biochemistry and to the Swiss Light Source Synchrotron in Villigen (Switzerland). We thank Steffen Schuessler and Ariane Fischer for their help with protein expression and purification. We thank Bastien Morlet for mass spectrometry analyses and IGBMC platforms for support. The work in the Conti lab was supported by funding from the Max-Planck-Gesellschaft, the European Commission (ERC Advanced Investigator Grants EXORICO and GOVERNA), the German Research Foundation (DFG SFB1035 and GRK1721), and Novo Nordisk Foundation (ExoAdapt). The work in the Séraphin lab was supported by funding from the Ligue Contre le Cancer (Equipe Labellisée 2020) [to B.S.], the Agence Nationale de la Recherche grant ANR-21-CE12-0003 [to F.M.], and the CERBM-IGBMC. This work of the Interdisciplinary Thematic Institute IMCBio, as part of the ITI 2021-2028 program of the University of Strasbourg, CNRS, and Inserm, was supported by IdEx Unistra (ANR-10-IDEX-0002), and by SFRI-STRAT'US project (ANR 20-SFRI-0012) and EUR IMCBio (ANR-17-EURE-0023) under the framework of the French Investments for the Future Program [to B.S.].

AUTHOR CONTRIBUTIONS

J.B. carried out the structural biology experiments and, together with S.O., J.A., and I.S., performed the *in vitro* biochemistry experiments in the lab of E.C. F.M., with the support of M.R. in the lab of B.S., performed biochemical and cellular assays. E.C., B.S., F.M., J.B, I.S., and J.A. wrote the manuscript.

DECLARATION OF INTERESTS

The authors declare no competing interests.

Received: August 9, 2022
Revised: October 27, 2022
Accepted: December 8, 2022
Published: December 30, 2022

REFERENCES

1. Chalabi Hagkarim, N., and Grand, R.J. (2020). The regulatory properties of the Ccr4-not complex. Cells *9*. https://doi.org/10.3390/cells9112379.
2. Ukleja, M., Valpuesta, J.M., Dziembowski, A., and Cuellar, J. (2016). Beyond the known functions of the CCR4-NOT complex in gene expression regulatory mechanisms: new structural insights to unravel CCR4-NOT mRNA processing machinery. Bioessays *38*, 1048–1058. https://doi.org/10.1002/bies.201600092.
3. Villanyi, Z., and Collart, M.A. (2016). Building on the Ccr4-not architecture. Bioessays *38*, 997–1002. https://doi.org/10.1002/bies.201600051.
4. Wahle, E., and Winkler, G.S. (2013). RNA decay machines: deadenylation by the Ccr4-not and Pan2-Pan3 complexes. Biochim. Biophys. Acta *1829*, 561–570. https://doi.org/10.1016/j.bbagrm.2013.01.003.
5. Daugeron, M.C., Mauxion, F., and Séraphin, B. (2001). The yeast POP2 gene encodes a nuclease involved in mRNA deadenylation. Nucleic Acids Res. *29*, 2448–2455. https://doi.org/10.1093/nar/29.12.2448.
6. Tucker, M., Valencia-Sanchez, M.A., Staples, R.R., Chen, J., Denis, C.L., and Parker, R. (2001). The transcription factor associated Ccr4 and Caf1 proteins are components of the major cytoplasmic mRNA deadenylase in Saccharomyces cerevisiae. Cell *104*, 377–386. https://doi.org/10.1016/s0092-8674(01)00225-2.
7. Eckmann, C.R., Rammelt, C., and Wahle, E. (2011). Control of poly(A) tail length. Wiley Interdiscip Rev RNA *2*, 348–361. https://doi.org/10.1002/wrna.56.
8. Passmore, L.A., and Coller, J. (2022). Roles of mRNA poly(A) tails in regulation of eukaryotic gene expression. Nat. Rev. Mol. Cell Biol. *23*, 93–106. https://doi.org/10.1038/s41580-021-00417-y.
9. Shirai, Y.T., Suzuki, T., Morita, M., Takahashi, A., and Yamamoto, T. (2014). Multifunctional roles of the mammalian CCR4-NOT complex in physiological phenomena. Front. Genet. *5*, 286. https://doi.org/10.3389/fgene.2014.00286.
10. Chalabi Hagkarim, N., Ryan, E.L., Byrd, P.J., Hollingworth, R., Shimwell, N.J., Agathanggelou, A., Vavasseur, M., Kolbe, V., Speiseder, T., Dobner, T., et al. (2018). Degradation of a novel DNA damage response protein, Tankyrase 1 binding protein 1, following adenovirus infection. J. Virol. *92*, 020344-e2117. https://doi.org/10.1128/JVI.02034-17.
11. Lau, N.C., Kolkman, A., van Schaik, F.M.A., Mulder, K.W., Pijnappel, W.W.M.P., Heck, A.J.R., and Timmers, H.T.M. (2009). Human Ccr4-Not complexes contain variable deadenylase subunits. Biochem. J. *422*, 443–453. https://doi.org/10.1042/BJ20090500.
12. Mauxion, F., Prève, B., and Séraphin, B. (2013). C2ORF29/CNOT11 and CNOT10 form a new module of the CCR4-NOT complex. RNA Biol. *10*, 267–276. https://doi.org/10.4161/rna.23065.
13. Chen, Y., Boland, A., Kuzuoğlu-Öztürk, D., Bawankar, P., Loh, B., Chang, C.T., Weichenrieder, O., and Izaurralde, E. (2014). A DDX6-CNOT1 complex and W-binding pockets in CNOT9 reveal direct links between miRNA target recognition and silencing. Mol. Cell *54*, 737–750. https://doi.org/10.1016/j.molcel.2014.03.034.
14. Mathys, H., Basquin, J., Ozgur, S., Czarnocki-Cieciura, M., Bonneau, F., Aartse, A., Dziembowski, A., Nowotny, M., Conti, E., and Filipowicz, W. (2014). Structural and biochemical insights to the role of the CCR4-NOT complex and DDX6 ATPase in microRNA repression. Mol. Cell *54*, 751–765. https://doi.org/10.1016/j.molcel.2014.03.036.
15. Basquin, J., Roudko, V.V., Rode, M., Basquin, C., Séraphin, B., and Conti, E. (2012). Architecture of the nuclease module of the yeast Ccr4-not complex: the Not1-Caf1-Ccr4 interaction. Mol. Cell *48*, 207–218. https://doi.org/10.1016/j.molcel.2012.08.014.
16. Chen, Y., Khazina, E., Izaurralde, E., and Weichenrieder, O. (2021). Crystal structure and functional properties of the human CCR4-CAF1 deadenylase complex. Nucleic Acids Res. *49*, 6489–6510. https://doi.org/10.1093/nar/gkab414.
17. Petit, A.P., Wohlbold, L., Bawankar, P., Huntzinger, E., Schmidt, S., Izaurralde, E., and Weichenrieder, O. (2012). The structural basis for the interaction between the CAF1 nuclease and the NOT1 scaffold of the human CCR4-NOT deadenylase complex. Nucleic Acids Res. *40*, 11058–11072. https://doi.org/10.1093/nar/gks883.
18. Fabian, M.R., Frank, F., Rouya, C., Siddiqui, N., Lai, W.S., Karetnikov, A., Blackshear, P.J., Nagar, B., and Sonenberg, N. (2013). Structural basis for

the recruitment of the human CCR4-NOT deadenylase complex by tristetraprolin. Nat. Struct. Mol. Biol. *20*, 735–739. https://doi.org/10.1038/nsmb.2572.

19. Rouya, C., Siddiqui, N., Morita, M., Duchaine, T.F., Fabian, M.R., and Sonenberg, N. (2014). Human DDX6 effects miRNA-mediated gene silencing via direct binding to CNOT1. RNA *20*, 1398–1409. https://doi.org/10.1261/rna.045302.114.
20. Leppek, K., Schott, J., Reitter, S., Poetz, F., Hammond, M.C., and Stoecklin, G. (2013). Roquin promotes constitutive mRNA decay via a conserved class of stem-loop recognition motifs. Cell *153*, 869–881. https://doi.org/10.1016/j.cell.2013.04.016.
21. Mauxion, F., Faux, C., and Séraphin, B. (2008). The BTG2 protein is a general activator of mRNA deadenylation. EMBO J. *27*, 1039–1048. https://doi.org/10.1038/emboj.2008.43.
22. Sgromo, A., Raisch, T., Bawankar, P., Bhandari, D., Chen, Y., Kuzuoğlu-Öztürk, D., Weichenrieder, O., and Izaurralde, E. (2017). A CAF40-binding motif facilitates recruitment of the CCR4-NOT complex to mRNAs targeted by Drosophila Roquin. Nat. Commun. *8*, 14307. https://doi.org/10.1038/ncomms14307.
23. Bhaskar, V., Roudko, V., Basquin, J., Sharma, K., Urlaub, H., Séraphin, B., et al. (2013). Structure and RNA-binding properties of the Not1-Not2-Not5 module of the yeast Ccr4-Not complex. Nat. Struct. Mol. Biol. *20*, 1281–1288. https://doi.org/10.1038/nsmb.2686.
24. Boland, A., Chen, Y., Raisch, T., Jonas, S., Kuzuoğlu-Öztürk, D., Wohlbold, L., Weichenrieder, O., and Izaurralde, E. (2013). Structure and assembly of the NOT module of the human CCR4-NOT complex. Nat. Struct. Mol. Biol. *20*, 1289–1297. https://doi.org/10.1038/nsmb.2681.
25. Buschauer, R., Matsuo, Y., Sugiyama, T., Chen, Y.H., Alhusaini, N., Sweet, T., Ikeuchi, K., Cheng, J., Matsuki, Y., Nobuta, R., et al. (2020). The Ccr4-Not complex monitors the translating ribosome for codon optimality. Science *368*, eaay6912. https://doi.org/10.1126/science.aay6912.
26. Absmeier, E., Chandrasekaran, V., O'Reilly, F.J., Stowell, J.A., Rappsilber, J., and Passmore, L.A. (2022). Specific recognition and ubiquitination of slow-moving ribosomes by human CCR4-NOT. Preprint at bioRxiv. https://doi.org/10.1101/2022.07.24.501325.
27. Bhaskar, V., Basquin, J., and Conti, E. (2015). Architecture of the ubiquitylation module of the yeast Ccr4-Not complex. Structure *23*, 921–928. https://doi.org/10.1016/j.str.2015.03.011.
28. Dimitrova, L.N., Kuroha, K., Tatematsu, T., and Inada, T. (2009). Nascent peptide-dependent translation arrest leads to Not4p-mediated protein degradation by the proteasome. J. Biol. Chem. *284*, 10343–10352. https://doi.org/10.1074/jbc.M808840200.
29. Bhandari, D., Raisch, T., Weichenrieder, O., Jonas, S., and Izaurralde, E. (2014). Structural basis for the Nanos-mediated recruitment of the CCR4-NOT complex and translational repression. Genes Dev. *28*, 888–901. https://doi.org/10.1101/gad.237289.113.
30. Bawankar, P., Loh, B., Wohlbold, L., Schmidt, S., and Izaurralde, E. (2013). NOT10 and C2orf29/NOT11 form a conserved module of the CCR4-NOT complex that docks onto the NOT1 N-terminal domain. RNA Biol. *10*, 228–244. https://doi.org/10.4161/rna.23018.
31. Raisch, T., Chang, C.T., Levdansky, Y., Muthukumar, S., Raunser, S., and Valkov, E. (2019). Reconstitution of recombinant human CCR4-NOT reveals molecular insights into regulated deadenylation. Nat. Commun. *10*, 3173. https://doi.org/10.1038/s41467-019-11094-z.
32. Gordon, D.E., Watson, A., Roguev, A., Zheng, S., Jang, G.M., Kane, J., Xu, J., Guo, J.Z., Stevenson, E., Swaney, D.L., et al. (2020). A quantitative genetic interaction map of HIV infection. Mol. Cell *78*, 197–209.e7. https://doi.org/10.1016/j.molcel.2020.02.004.
33. Du, H., Chen, C., Wang, Y., Yang, Y., Che, Z., Liu, X., Meng, S., Guo, C., Xu, M., Fang, H., et al. (2020). RNF219 interacts with CCR4-NOT in regulating stem cell differentiation. J. Mol. Cell Biol. *12*, 894–905. https://doi.org/10.1093/jmcb/mjaa061.
34. Färber, V., Erben, E., Sharma, S., Stoecklin, G., and Clayton, C. (2013). Trypanosome CNOT10 is essential for the integrity of the NOT deadenylase complex and for degradation of many mRNAs. Nucleic Acids Res. *41*, 1211–1222. https://doi.org/10.1093/nar/gks1133.
35. Andrade, M.A., Petosa, C., O'Donoghue, S.I., Müller, C.W., and Bork, P. (2001). Comparison of ARM and HEAT protein repeats. J. Mol. Biol. *309*, 1–18. https://doi.org/10.1006/jmbi.2001.4624.
36. D'Andrea, L.D., and Regan, L. (2003). TPR proteins: the versatile helix. Trends Biochem. Sci. *28*, 655–662. https://doi.org/10.1016/j.tibs.2003.10.007.
37. Ponting, C.P. (2000). Novel eIF4G domain homologues linking mRNA translation with nonsense-mediated mRNA decay. Trends Biochem. Sci. *25*, 423–426. https://doi.org/10.1016/s0968-0004(00)01628-5.
38. Conti, E., Uy, M., Leighton, L., Blobel, G., and Kuriyan, J. (1998). Crystallographic analysis of the recognition of a nuclear localization signal by the nuclear import factor karyopherin alpha. Cell *94*, 193–204. https://doi.org/10.1016/s0092-8674(00)81419-1.
39. Tunyasuvunakool, K., Adler, J., Wu, Z., Green, T., Zielinski, M., Žídek, A., Bridgland, A., Cowie, A., Meyer, C., Laydon, A., et al. (2021). Highly accurate protein structure prediction for the human proteome. Nature *596*, 590–596. https://doi.org/10.1038/s41586-021-03828-1.
40. Evans, R., O'Neill, M., Pritzel, A., Antropova, N., Senior, A., Green, T., Žídek, A., Bates, R., Blackwell, S., Yim, J., et al. (2021). Protein complex prediction with AlphaFold-Multimer. Preprint at bioRxiv. https://doi.org/10.1101/2021.10.04.463034.
41. De Franco, E., Watson, R.A., Weninger, W.J., Wong, C.C., Flanagan, S.E., Caswell, R., Green, A., Tudor, C., Lelliott, C.J., Geyer, S.H., et al. (2019). A specific CNOT1 mutation results in a novel syndrome of pancreatic agenesis and holoprosencephaly through impaired pancreatic and neurological development. Am. J. Hum. Genet. *104*, 985–989. https://doi.org/10.1016/j.ajhg.2019.03.018.
42. Kruszka, P., Berger, S.I., Weiss, K., Everson, J.L., Martinez, A.F., Hong, S., Anyane-Yeboa, K., Lipinski, R.J., and Muenke, M. (2019). A CCR4-NOT transcription complex, subunit 1, CNOT1, variant associated with holoprosencephaly. Am. J. Hum. Genet. *104*, 990–993. https://doi.org/10.1016/j.ajhg.2019.03.017.
43. Chen, A., Li, J., Song, L., Ji, C., Böing, M., Chen, J., and Brand-Saberi, B. (2017). GGNBP2 is necessary for testis morphology and sperm development. Sci. Rep. *7*, 2998. https://doi.org/10.1038/s41598-017-03193-y.
44. Liu, L., He, Y., Guo, K., Zhou, L., Li, X., Tseng, M., Cai, L., Lan, Z.J., Zhou, J., Wang, H., and Lei, Z. (2017). Ggnbp2-Null mutation in mice leads to male infertility due to a defect at the spermiogenesis stage. Am. J. Pathol. *187*, 2508–2519. https://doi.org/10.1016/j.ajpath.2017.07.016.
45. Liu, J., Liu, L., Yagüe, E., Yang, Q., Pan, T., Zhao, H., Hu, Y., and Zhang, J. (2019). GGNBP2 suppresses triple-negative breast cancer aggressiveness through inhibition of IL-6/STAT3 signaling activation. Breast Cancer Res. Treat. *174*, 65–78. https://doi.org/10.1007/s10549-018-5052-z.
46. Xu, X., Zhu, Z., Xu, Y., Tian, S., Jiang, Y., and Zhao, H. (2020). Effects of zinc finger protein 403 on the proliferation, migration and invasion abilities of prostate cancer cells. Oncol. Rep. *44*, 2455–2464. https://doi.org/10.3892/or.2020.7786.
47. Zhan, A., Lei, B., Wu, H., Wen, Y., Zheng, L., Wang, S., Wan, X., and Wei, Z. (2017). GGNBP2 suppresses the proliferation, invasion, and migration of human glioma cells. Oncol. Res. *25*, 831–842. https://doi.org/10.3727/096504016X14816726393937.
48. Zhu, Z., Lou, C., Zheng, Z., Zhu, R., Tian, S., Xie, C., and Zhao, H. (2017). ZFP403, a novel tumor suppressor, inhibits the proliferation and metastasis in ovarian cancer. Gynecol. Oncol. *147*, 418–425. https://doi.org/10.1016/j.ygyno.2017.08.025.
49. Adams, P.D., Afonine, P.V., Bunkóczi, G., Chen, V.B., Davis, I.W., Echols, N., Headd, J.J., Hung, L.W., Kapral, G.J., Grosse-Kunstleve, R.W., et al. (2010). PHENIX: a comprehensive Python-based system for

macromolecular structure solution. Acta Crystallogr. D Biol. Crystallogr. *66*, 213–221. https://doi.org/10.1107/S0907444909052925.

50. Sheldrick, G.M. (2010). Experimental phasing with SHELXC/D/E: combining chain tracing with density modification. Acta Crystallogr. D Biol. Crystallogr. *66*, 479–485. https://doi.org/10.1107/S0907444909038360.

51. Cowtan, K. (2006). The Buccaneer software for automated model building. 1. Tracing protein chains. Acta Crystallogr. D Biol. Crystallogr. *62*, 1002–1011. https://doi.org/10.1107/S0907444906022116.

52. Emsley, P., Lohkamp, B., Scott, W.G., and Cowtan, K. (2010). Features and development of Coot. Acta Crystallogr. D Biol. Crystallogr. *66*, 486–501. https://doi.org/10.1107/S0907444910007493.

53. McCoy, A.J., Grosse-Kunstleve, R.W., Adams, P.D., Winn, M.D., Storoni, L.C., and Read, R.J. (2007). Phaser crystallographic software. J. Appl. Crystallogr. *40*, 658–674. https://doi.org/10.1107/S0021889807021206.

54. Schorb, M., Haberbosch, I., Hagen, W.J.H., Schwab, Y., and Mastronarde, D.N. (2019). Software tools for automated transmission electron microscopy. Nat. Methods *16*, 471–477. https://doi.org/10.1038/s41592-019-0396-9.

55. Zivanov, J., Nakane, T., Forsberg, B.O., Kimanius, D., Hagen, W.J., Lindahl, E., and Scheres, S.H. (2018). New tools for automated high-resolution Cryo-EM structure determination in RELION-3. Elife *7*. https://doi.org/10.7554/eLife.42166.

56. Punjani, A., Rubinstein, J.L., Fleet, D.J., and Brubaker, M.A. (2017). cryoSPARC: algorithms for rapid unsupervised cryo-EM structure determination. Nat. Methods *14*, 290–296. https://doi.org/10.1038/nmeth.4169.

57. Zheng, S.Q., Palovcak, E., Armache, J.P., Verba, K.A., Cheng, Y., and Agard, D.A. (2017). MotionCor2: anisotropic correction of beam-induced motion for improved cryo-electron microscopy. Nat. Methods *14*, 331–332. https://doi.org/10.1038/nmeth.4193.

58. Rohou, A., and Grigorieff, N. (2015). CTFFIND4: Fast and accurate defocus estimation from electron micrographs. J. Struct. Biol. *192*, 216–221. https://doi.org/10.1016/j.jsb.2015.08.008.

59. Bepler, T., Morin, A., Rapp, M., Brasch, J., Shapiro, L., Noble, A.J., and Berger, B. (2019). Positive-unlabeled convolutional neural networks for particle picking in cryo-electron micrographs. Nat. Methods *16*, 1153–1160. https://doi.org/10.1038/s41592-019-0575-8.

60. Zhang, K. (2016). Gctf: real-time CTF determination and correction. J. Struct. Biol. *193*, 1–12. https://doi.org/10.1016/j.jsb.2015.11.003.

61. Sanchez-Garcia, R., Gomez-Blanco, J., Cuervo, A., Carazo, J.M., Sorzano, C.O.S., and Vargas, J. (2021). DeepEMhancer: a deep learning solution for cryo-EM volume post-processing. Commun. Biol. *4*, 874. https://doi.org/10.1038/s42003-021-02399-1.

62. Pettersen, E.F., Goddard, T.D., Huang, C.C., Couch, G.S., Greenblatt, D.M., Meng, E.C., and Ferrin, T.E. (2004). UCSF Chimera–a visualization system for exploratory research and analysis. J. Comput. Chem. *25*, 1605–1612. https://doi.org/10.1002/jcc.20084.

63. Rigaut, G., Shevchenko, A., Rutz, B., Wilm, M., Mann, M., and Séraphin, B. (1999). A generic protein purification method for protein complex characterization and proteome exploration. Nat. Biotechnol. *17*, 1030–1032. https://doi.org/10.1038/13732.

64. Kabsch, W. (2010). Integration, scaling, space-group assignment and post-refinement. Acta Crystallogr. D Biol. Crystallogr. *66*, 133–144. https://doi.org/10.1107/S0907444909047374.

65. Karplus, P.A., and Diederichs, K. (2012). Linking crystallographic model and data quality. Science *336*, 1030–1033. https://doi.org/10.1126/science.1218231.

66. Rosenthal, P.B., and Henderson, R. (2003). Optimal determination of particle orientation, absolute hand, and contrast loss in single-particle electron cryomicroscopy. J. Mol. Biol. *333*, 721–745. https://doi.org/10.1016/j.jmb.2003.07.013.

Please cite this article in press as: Mauxion et al., The human CNOT1-CNOT10-CNOT11 complex forms a structural platform for protein-protein interactions, Cell Reports (2022), https://doi.org/10.1016/j.celrep.2022.111902

STAR★METHODS

KEY RESOURCES TABLE

REAGENT or RESOURCE	SOURCE	IDENTIFIER
Antibodies		
Rabbit polyclonal anti-CNOT10	Proteintech	Cat# 15938-1-AP; RRID:AB_2229678
Mouse monoclonal anti-GFP (clone JL-8)	Takara	Cat# 632381; RRID:AB_2313808
Rabbit polyclonal anti-CNOT11	(Mauxion et al.)[12]	N/A
Rabbit polyclonal anti-CNOT7	(Mauxion et al.)[12]	N/A
Bacterial and virus strains		
Escherichia coli BL21 (DE3) STAR pRARE	Stratagene	N/A
Escherichia coli B834	Sigma-Aldrich	Cat# 69041
Chemicals, peptides, and recombinant proteins		
Protein Assay Dye Reagent Concentrate	Bio-Rad	Cat# 5000006
ChromoTek GFP-Trap Magnetic Agarose	Proteintech	Cat# gtma
ChromoTek GFP-Trap Magnetic Particles M-270	Proteintech	Cat# gtd
Immobilon Western HRP Substrate	MerckMillipore	Cat# WBKLS0100
Luminata Crescendo Western HRP Substrate	MerckMillipore	Cat# WBLUR0100
IgG Sepharose 6 Fast Flow Affinity Resin	Cytiva	Cat# 17096901
AcTEV protease	Invitrogen	Cat# 12575-015
Calmodulin Affinity Resin	Agilent	Cat# 214303-52
cOmplete protease inhibitor cocktail, EDTA-free	Roche	SKU# 5056489001
H. sapiens CNOT1N (residues 1-687) + N-terminal His-SUMO-tag fusion protein cleavable with SENP2	This study	N/A
H. sapiens CNOT10 (residues 1-714) + N-terminal His-Thioredoxin-tag fusion proteins cleavable with 3C protease	This study	N/A
H. sapiens CNOT11 (residues 61-510) + N-terminal His-Thioredoxin-tag fusion proteins cleavable with 3C protease	This study	N/A
H. sapiens CNOT11C (residues 325-510) + N-terminal His-SUMO-tag fusion protein cleavable with SENP2	This study	N/A
H. sapiens CNOT11C-GGNBP2 (residues 638-673) + N-terminal His-SUMO-tag fusion protein cleavable with SENP2	This study	N/A
SENP	Sigma-Aldrich	Cat# SAE0067
3C Protease	Sigma-Aldrich	Cat# SAE0045
Critical commercial assays		
Effectene Transfection Reagent	Qiagen	Cat# 301427
Beta-Glo Assay System	Promega	Cat# E4720
Deposited data		
$CNOT1_N$-CNOT10-CNOT11	This paper	PDB: 8BFI
$CNOT11_C$	This paper	PDB: 8BFH
partial $CNOT11_C$-GGNBP2 (residues 638-673)	This paper	PDB: 8BFJ
Experimental models: Cell lines		
Human embryonic kidney 293 (HEK293)	ATCC	CRL1573; RRID:CVCL_0045

(*Continued on next page*)

Please cite this article in press as: Mauxion et al., The human CNOT1-CNOT10-CNOT11 complex forms a structural platform for protein-protein interactions, Cell Reports (2022), https://doi.org/10.1016/j.celrep.2022.111902

Continued

REAGENT or RESOURCE	SOURCE	IDENTIFIER
Experimental models: Organisms/strains		
S. cerevisiae diploid strain Y187/L40: MATα/MATa, ade2-101/ade2, his3-200/his3Δ200, leu2-3,-112/leu2-3,-112, lys2- 801am::LYS2::(lexAop)4-HIS3/LYS2, MEL1/?, met-/MET, trp1-901/trp1-901, gal4Δ/gal4- 542, gal80Δ/gal80-538, ura3-52::URA3::GAL1UAS-GAL1TATA-lacZ/URA3::(lexAop)8- lacZ	Hybrigenics	N/A
Oligonucleotides		
See Table S3	N/A	N/A
Recombinant DNA		
See Table S2	N/A	N/A
Software and algorithms		
Proteome Discoverer 2.2	ThermoFisher Scientific	RRID:SCR_014477
Phenix.refine	(Adams et al.)[49]	RRID:SCR_016736
AlphaFold	(Tunyasuvunakool et al.)[39]	https://alphafold.ebi.ac.uk/
SHELX C/D/E	(Sheldrick et al.)[50]	RRID:SCR_014220
Buccaneer	(Cowtan et al.)[51]	RRID:SCR_014221
Coot	(Emsley et al.)[52]	RRID:SCR_014222
Phaser	(McCoy et al.)[53]	RRID:SCR_014219
SerialEM	(Schorb et al.)[54]	RRID:SCR_017293
Relion 3.1	(Zivanov et al.)[55]	RRID:SCR_016274
cryoSPARC	(Punjani et al.)[56]	RRID:SCR_016501
MotionCor2	(Zheng et al.)[57]	RRID:SCR_016499
CTFFIND4	(Rohou et al.)[58]	RRID:SCR_016732
TOPAZ	(Bepler et al.)[59]	N/A
GCTF	(Zhang et al.)[60]	RRID:SCR_016500
Deep EMhancer	(Sanchez-Garcia et al.)[61]	N/A
UCSF Chimera	(Pettersen et al.)[62]	RRID:SCR_004097
Other		
Superdex 200 Increase 10/300 GL	Cytiva	28990944

RESOURCE AVAILABILITY

Lead contact

Further information and requests for resources and reagents should be directed to and will be fulfilled by the lead contact, Elena Conti conti@biochem.mpg.de.

Materials availability

This study did not generate new unique reagents.

Data and code availability

- The coordinates and the structure factors have been deposited in the Protein Data Bank (PDB) under the accession numbers: PDB: 8BFI ($CNOT1_N$-CNOT10-CNOT11), PDB: 8BFH ($CNOT11_C$), PDB: 8BHJ ($CNOT11_C$-GGNBP2 (residues 638-673, partial model)), Data are available at time of publication.
- This paper does not report original code.
- Any additional information required to reanalyse the data reported in this work/paper is available from the lead contact upon request.

Please cite this article in press as: Mauxion et al., The human CNOT1-CNOT10-CNOT11 complex forms a structural platform for protein-protein interactions, Cell Reports (2022), https://doi.org/10.1016/j.celrep.2022.111902

EXPERIMENTAL MODEL AND SUBJECT DETAILS

All bacterial and eukaryotic cell lines in this study were used for protein production for *in vitro* experiments. Yeast strains were used for yeast two-hybrid screens. All cell types are listed in the key resources table. Handling information pertinent to each cell type is described in detail in the method details section.

METHOD DETAILS

Molecular cloning

Constructions (Table S2) used in this study were obtained by standard cloning strategies. Clones were verified by Sanger sequencing when a PCR step was involved during their construction. Oligonucleotides used for this study are listed in Table S3.

Cell transfection

HEK293 cells (ATCC CRL-1573) were maintained in DMEM medium containing 4.5 g/L glucose, GlutaMAX, 10% fetal calf serum and 40 μg/mL gentamicin. Cells were transfected with Effectene transfection reagent (Qiagen) per the manufacturer's instruction and processed 24- to 48-hours post-transfection.

Protein co-immunoprecipitation and western blotting

Co-immunoprecipitation experiments were performed using GFP-Trap magnetic agarose or magnetic particles M-270 beads (Chromotek) as recommended by the manufacturer. Specifically, cells grown in 10 cm dishes were lysed after transfection in 200 μL lysis buffer (10 mM Tris-HCl pH 8.0, 150 mM NaCl, 0.5 mM EDTA, 0.5% Igepal CA-630) supplemented with protease inhibitors (10 mM phenylmethylsulfonyl fluoride (PMSF) and 1X Complete Protease Inhibitor Cocktail EDTA-free, Roche). After centrifugation at 20,000 g for 10 min at 4°C, 300 μL of wash buffer (10 mM Tris-HCl pH 7.5, 150 mM NaCl, 0.5 mM EDTA supplemented with protease inhibitors) was added to the supernatant and protein concentration was determined with Protein Assay Dye Reagent Concentrate (Bio-Rad). Cell lysates corresponding to equal protein amount were then incubated with 10 μL GFP-Trap magnetic beads for 1 h at 4°C mixing by rotation. After recovery, beads were washed three times with 500 μL wash buffer and eluted 10 min at 95°C with 60 μL Laemmli sample buffer (60 mM Tris-HCl pH 6.8, 10% glycerol, 0.002% bromophenol blue, 2% sodium dodecyl sulfate and 5% dithiothreitol).

Western blotting was performed using standard procedures and blots visualized with Amersham Imager 600 (GE Healthcare) or Amersham ImageQuant 800 (Cytiva). GFP fusion proteins were revealed with mouse monoclonal antibody anti-GFP (JL-8, Clontech) used at 1/1000 or 1/5000 dilution, endogenous CNOT10, CNOT7 and CNOT11 proteins were revealed with rabbit polyclonal anti-CNOT10 antibody (15938-1- AP, Proteintech) used at 1/1000 dilution or with home-made rabbit anti-CNOT7 or anti-CNOT11 antiserum used at 1/1000 dilution, respectively. HRP revelation was performed with the Immobilon or Luminata Crescendo Western HRP Substrates (Millipore).

GFP-tagged protein immunoprecipitation for mass spectrometry analysis

For mass spectrometry analysis, GFP-tagged immunoprecipitations were performed using GFP-Trap magnetic beads (Chromotek) as reported above with minor changes. Briefly, after the incubation period of 1 hour, the GFP-Trap magnetic beads were first washed twice with wash buffer (10 mM Tris-HCl pH 7.5, 150 mM NaCl and 0.5 mM EDTA) supplemented with 0.25% Igepal CA-630 and then washed three times with wash buffer only. After transfer to a new tube, the magnetic beads were processed for mass spectrometry analysis as described below.

TAP-tagged protein purification

The TAP purification procedure[63] was adapted to mammalian cell cultures as previously published.[12] Specifically, HEK293 cells grown in 10 cm dishes (10 dishes per TAP construction) were lysed in 4 mL IPP150 buffer (10 mM Tris-HCl pH 8, 150 mM NaCl) supplemented with 1% Igepal CA-630 and protease inhibitors (10 mM PMSF and 1X Complete Protease Inhibitor Cocktail EDTA-free) and lysates were subjected to two consecutive centrifugations at 20,000 g for 15 min at 4°C. Cell supernatants were then incubated with 100 μL IgG Sepharose 6 Fast Flow beads (GE Healthcare) for 2 hours at 4°C and the beads were washed with 10 mL IPP150 buffer supplemented with 0.1% Igepal CA-630 followed by a wash with 5 mL TEV cleavage buffer (10 mM Tris-HCl pH 8, 150 mM NaCl, 0.1% Igepal CA-630, 0.5 mM EDTA, 1 mM DTT and protease inhibitors). Beads were resuspended in 1 mL of TEV cleavage buffer, 10 μL AcTEV protease (Invitrogen) was added and beads were incubated 2 hours at 16°C. After TEV cleavage, eluates were recovered and supplemented with 3 mL of Calmodulin Binding Buffer (10 mM Tris-HCl pH 8, 150 mM NaCl, 1 mM MgAc, 1 mM Imidazole, 2 mM CaCl2, 0.1% Igepal CA-630, 10 mM β-mercaptoethanol and protease inhibitors) and 3 μL of 1M CaCl2. These samples were then incubated with Calmodulin Affinity Resin (Agilent Technologies) for 1 hour at 4°C. The beads were washed with 10 mL Calmodulin Binding Buffer and eluted in 5 fractions of 100 μL with Calmodulin Elution Buffer (10 mM Tris-HCl pH 8, 150 mM NaCl, 1 mM MgAc, 5 mM EGTA, 0.1% Igepal CA-630, 10 mM β-mercaptoethanol). Eluates were first analyzed by western blotting, which confirmed the presence of CNOT11 derivatives in fractions 2 to 5. These fractions were then pooled and processed for mass spectrometry analysis after TCA precipitation.

Mass spectrometry

Protein mixtures were denatured, reduced and alkylated before overnight trypsin digestion. Peptide mixtures were then desalted, dried and analyzed using an Ultimate 3000 nano-RSLC.

(Thermo Scientific, San Jose California) coupled in line with an LTQ-Orbitrap ELITE mass spectrometer via a nano-electrospray ionization source (Thermo Scientific, San Jose California). Tryptic peptides (in triplicate) were loaded on a C18 Acclaim PepMap100 trap-column and then separated on a C18 Accucore nano-column at a flow rate of 200 nL/min for 2 h. The mass spectrometer was operated in positive ionization mode, in DDA (Data- Dependent Acquisition) with survey scans from m/z 350-1500 acquired in the Orbitrap at a resolution of 120,000 at m/z 400. The 20 most intense peaks from survey scans were selected for further fragmentation in the Linear Ion Trap with an isolation window of 2.0 Da and were fragmented by Collision-Induced Dissociation with normalized collision energy of 35%. Unassigned and single charged states were rejected. The Ion Target Value for the survey scans (in the Orbitrap) and the MS2 mode (in the Linear Ion Trap) were set to 1E6 and 5E3, respectively, and the maximum injection time was set to 100 ms for both scan modes. Dynamic exclusion was used. Exclusion duration was set to 20 s, repeat count was set to 1 and exclusion mass width was ±10 ppm.

Proteins were identified by database searching using SequestHT (Thermo Fisher Scientific) with Proteome Discoverer 2.2 software (PD2.2, Thermo Fisher Scientific) on Homo sapiens database (Swissprot, reviewed, release 2019_07_16, 20286 entries). Precursor and fragment mass tolerances were set at 7 ppm and 0.6 Da, respectively, and up to 2 missed cleavages were allowed. Oxidation (M) was set as variable modification, and carbamidomethylation (C) as fixed modification. Peptides were filtered with a false discovery rate (FDR) at 1%, rank 1 and proteins were identified with a minimum of 2 unique peptides.

Yeast two-hybrid screen and assays

A two-hybrid screen of a human placenta cDNA library with a LexA-Binding-Domain- CNOT11(323-510) fusion bait was performed by Hybrigenics. For subsequent tests, a host diploid yeast strain.

Y187/L40 (MATα/MATa, ade2-101/ade2, his3-200/his3Δ200, leu2-3, −112/leu2-3, −112, lys2- 801am:LYS2::(lexAop)4-HIS3/LYS2, MEL1/?, met-/MET, trp1-901/trp1-901, gal4Δ/gal4- 542, gal80Δ/gal80-538, ura3-52:URA3:GAL1UAS-GAL1TATA-lacZ/URA3::(lexAop)8- lacZ) was transformed simultaneously with the LexA-Binding-Domain and Gal4-Activating- Domain-derived plasmids by standard LiAc procedure. Interaction between the different chimeric proteins was monitored by β-galactosidase production using the Beta-Glo Assay System (Promega). For each protein pair, three yeast cultures were seeded from different colonies (2 transformants/culture) and grown in -Leu -Trp selective media to low density (OD600 of 0.1–1.0). Cultures were diluted to an OD600 of 0.1 in a final volume of 50 μL, 50 μL of Beta-Glo Reagent (Promega) was then added and the reactions were incubated at room temperature for 60 min after which light production was quantitated in a luminometer Centro XS3 LB 960 (Berthold).

Purification of recombinant proteins

All recombinant proteins were cloned and expressed in *E. coli* either as individual components or by co-expression. Human $CNOT1_N$ (residues 1-687) was cloned as an N-terminal His-SUMO-tag fusion protein cleavable with SENP2 while CNOT10 (1-714) and CNOT11 (61-510) were cloned into a bicistronic vector as N-terminal His-Thioredoxin-tag fusion proteins cleavable with 3C protease. Proteins were expressed separately in BL21(DE3) STAR pRARE (Stratagene) in Terrific Broth (TB) medium. Cells were mixed and resuspended in lysis buffer (50 mM NaH2PO4 pH 7.5, 150 mM NaCl, 40 mM imidazole, 5 mM β-Mercaptoethanol) supplemented with 1 mg of DNase I, 20 mM MgSO4 and 1 mM PMSF and lysed by sonication. The complex was purified using Nickel-based affinity chromatography followed by tag cleavage with SENP2 and 3C protease at 4°C for 4 hours. Upon dilution, the complex was further purified with an ion-exchange chromatography column at pH 8.0 (Heparin, GE healthcare) and a size-exclusion chromatography (Superdex 200) in size-exclusion buffer (Tris 20 mM pH 8.0, 150 mM NaCl and 2 mM DDT). The partial Seleno-methionine substituted complex was purified following the same procedure but using a pellet of CNOT1(1-687) which was grown using a B834 *E. coli* host strain in a minimal medium containing L-Seleno-methionine (50 mg/mL).

Human $CNOT11_C$ (residues 323-510) was cloned as an N-terminal His-SUMO-tag fusion protein cleavable with SENP2. The protein was expressed using a B834 *E. coli* host strain in a minimal medium containing L-Seleno-methionine (50 mg/mL) separately in BL21(DE3) STAR pRARE (Stratagene) in Terrific Broth (TB) medium. Cells were mixed and resuspended in lysis buffer (50 mM NaH2PO4 pH 7.5, 150 mM NaCl, 40 mM imidazole, 5 mM β-Mercaptoethanol) supplemented with 1 mg of DNase I, 20 mM MgSO4 and 1 mM PMSF and lysed by sonication. The complex was purified using Nickel-based affinity chromatography followed by tag cleavage with SENP2. The protein was further purified with a size-exclusion chromatography (Superdex 200) in size-exclusion buffer (Tris 20 mM pH 8.0, 150 mM NaCl and 2 mM DDT). The protein was concentrated to 15 mg/mL.

For co-crystallization purposes, human $CNOT11_C$ was co-expressed with GGNBP2 (residues 638-673) cloned as an N-terminal His-SUMO-tag fusion protein cleavable with SENP2. The complex was expressed in BL21(DE3) STAR pRARE (Stratagene) in Terrific Broth (TB) medium. Cells were mixed and resuspended in lysis buffer (50 mM NaH2PO4 pH 7.5, 150 mM NaCl, 40 mM imidazole, 5 mM β-Mercaptoethanol) supplemented with 1 mg of DNase I, 20 mM MgSO4 and 1 mM PMSF and lysed by sonication. The CNOT11C - GGNBP2 (residues 638-673) complex was purified using Nickel-based affinity chromatography followed by tag cleavage with SENP2. The complex was further purified with a size-exclusion chromatography (Superdex 200) in size-exclusion buffer (Tris 20 mM pH 8.0, 150 mM NaCl and 2 mM DDT). The complex was concentrated to 17 mg/mL.

Crystallization and structure determination

The $CNOT1_N$-CNOT10-CNOT11 complex was concentrated to 11 mg/mL. Crystals were grown at 19°C by hanging-drop vapor diffusion from drops formed by equal volumes of protein and of crystallization solution (5% (w/v) PEG 3500, 2% (v/v) isopropanol, 0.1 M MES pH 5.5). Prior to flash freezing in liquid nitrogen, the crystals were briefly soaked in mother liquor containing 28% (v/v) ethylene glycol. A single-wavelength anomalous diffraction experiment from Selenium (S-SAD) was performed at the macromolecular crystallography super-bending magnet beamline X06DA (PXIII) at the Swiss Light Source (Villigen, Switzerland). On a single crystal, 7 × 360° data sets were collected at 100 K at a wavelength of 0.977Å with 0.5° oscillation 0.1 s exposure in different orientations of a multi-axis goniometer. The data were processed using XDS and scaled and merged with XSCALE.[64] The high-resolution data cutoff was based on the statistical indicators CC1/2 and CC*.[65] Substructure determination and phasing were performed with SHELXC/D/E using the HKL2MAP interface.[50] The successful SHELXD substructure solution, in a search for 15 Se sites, had a CCall and a CCweak of 43 and 20, respectively. Density modification resulted in a clear separation of hands. The initial map was obtained using the phasing pipeline CRANK. Additionally, a single-wavelength anomalous diffraction experiment from intrinsic Sulfur atoms (S-SAD) was performed on the native complex to locate the sulfur atoms. On a single crystal, 6 × 360° datasets were collected at 100 K at a wavelength of 2.066Å with 0.5° oscillation 0.1 s exposure in different orientations of a multi-axis goniometer. The data were processed as described above. The position of the sulfur atoms was calculated using the ANODE. An initial model was built automatically with BUCCANEER[51] and extended manually in the experimental electron density in COOT[52] and refined with phenix.refine.[49]

Crystals of $CNOT11_C$ were grown at 19°C by hanging-drop vapor diffusion from drops formed by equal volumes of protein and of crystallization solution (11% (w/v) PEG 3500, 0.2M Ammonium acetate, 0.1 M MES pH 5.5). Prior to flash freezing in liquid nitrogen, the crystals were briefly soaked in mother liquor containing 28% (v/v) ethylene glycol. A single-wavelength anomalous diffraction experiment from Selenium (S-SAD) was performed at the macromolecular crystallography super-bending magnet beamline X06DA (PXIII) at the Swiss.

Light Source (Villigen, Switzerland). Data processing, phasing, model building and refinement were carried out as described above.

Crystals of $CNOT11_C$-GGNBP2 (residues 638-673) were grown at 19°C by hanging-drop vapor diffusion from drops formed by equal volumes of protein and of crystallization solution (1.5 M ammonium sulfate 1.5M, MPD 5% (w/v), 0.05 M Tris pH 8.0). Prior to flash freezing in liquid nitrogen, the crystals were briefly soaked in mother liquor containing 28% (v/v) ethylene glycol. A single-wavelength diffraction experiment was performed at the macromolecular crystallography beamline X10SA (PXII) at the Swiss Light Source (Villigen, Switzerland). Datasets were collected at 100 K at a wavelength of 1.00Å with 0.5° oscillation 0.1 s exposure. The data were processed as described above. Phasing was performed by molecular replacement using Phaser[53] with CNOT11C (as a search model). The model was built and refined against the native data as described above.

Cryo-EM sample preparation and data collection

The sample was diluted to a concentration of 0.25 mg/mL. For cryo-EM sample preparation, 4.0 μL of the purified complex were applied to glow discharged Quantifoil 2/1 grids, blotted for 3.5 s with force '4' in a Vitrobot Mark IV (Thermo Fisher) at 100% humidity and 4°C, and plunge vitrified in liquid ethane cooled by liquid nitrogen.

Electron micrographs were acquired with a FEI Titan Krios transmission electron microscope (ThermoFisher) using SerialEM software.[54] Movie frames were recorded at a nominal magnification of 81,000× (calibrated physical pixel size: 1.06Å/px) using a K2 direct electron detector (Gatan) and a GIF quantum energy filter (Gatan) at 20 eV slit width. The total electron dose of approximately 47 electrons per $Å^2$ was distributed over 35 frames and 3281 micrographs were collected.

Cryo-EM data processing

The collected data were processed in RELION 3.1[55] and cryoSPARC.[56]

To correct for beam-induced motions, raw movie frames were aligned using MotionCor2.[57] The aligned micrographs were imported into cryoSPARC and the per-micrograph contrast transfer function (CTF) parameters were estimated using CTFFIND4.[58] Initial particle candidates were selected using TOPAZ,[59] extracted with a box size of 256 px, and subjected to several rounds of 2D classification. The coordinates of the cleaned particle stack were exported to RELION 3.1. In RELION, CTF parameters were refined using GCTF.[60] Particles were re-extracted from aligned, exposure-weighted micrographs with a box size of 256 px. Reference-free 2D classification and two rounds of 3D classification using a 60 Å low-pass filtered starting model from a cryoSPARC *ab initio* reconstruction resulted in a 3D reconstruction from 222,742 particles. This subset of particles was subjected to CTF refinement (per-particle defocus, per-micrograph beam-tilt, and astigmatism estimation) followed by Bayesian particle polishing. After automatic b-factor sharpening (−116.42) in the RELION post-processing routine[55] the reconstruction reached a nominal global resolution of 3.8 Å according to the Fourier shell correlation (FSC) cut-off criterion for the independent half-maps of 0.143.[66] The independent half-maps were subjected to DeepEMhancer[61] and the resulting map was used for visualization and docking of the crystal structure.

The crystal structure of $CNOT1_N$-CNOT10-$CNOT11_{N-M}$ was docked by rigid-body fitting in UCSF chimera.[62]